Aalto University School of Science and Technology
CFD-group/ Department of Applied Mechanics

MEMO No CFD/MECHA-9-2010 DATE: October 4, 2010

TITLE

Large eddy simulations of mixing planar jets in a ventilated room

AUTHOR(S)
Tomas Brockmann

ABSTRACT

The work on simulation of mixing of planar jets in a room has been continued. Earlier large eddy simulations did not produce adequate results, because one jet eventually pushed the other jet away. In this work velocity fluctuations have been applied to the inflow. Most of the simulation work is about testing turbulence models and discretization schemes of the momentum equation. The open source finite-volume code OpenFOAM-1.5 has been used in the simulations.

MAIN RESULT

The simulation results are improved, but the flow could not be predicted accurately enough. Modelling strategy still needs reconsideration.

PAGES
22

KEY WORDS
large-eddy simulation method, OpenFOAM, room ventilation, mixing planar jets

APPROVED BY

Timo Siikonen October 4, 2010

Contents

Abstract

We have studied the mixing of planar ventilation jets in a three dimensional room. The simulation is done with the finite-volume method using OpenFOAM code. Turbulence effects are included by applying the large-eddy simulation method. This is an interesting alternative, because Reynolds-Averaged Navier-Stokes simulations have produced unrealistic results. For the time discretization a second-order accurate backward method has been used and for the spatial discretization comparisons have been made between a second-order central difference as well as some more stable but less accurate schemes. Comparisons between different turbulence models have also been made. Maintaining balance between the interacting jets has been a problem with LES in our earlier simulations. The situation depends on the simulation parameters and modelling choices.

1 Introduction

In this work we have studied the application of a large-eddy simulation method (LES) to an indoor ventilation flow problem. In LES the large scale flow is solved time accurately, and only the subgrid-scale turbulence influence to the flow is modelled. This allows a solution of flow structures, which are not fully laminar or turbulent and can only be found in time dependent modes. The case of interest is an office room with two ventilation beams on the roof. The beams produce somewhat planar jets along the ceiling. Most interest is placed on the behaviour of the impinging jets.

In our ealier work it was learned that the traditional time-averaged turbulence models (RANS) do not produce realistic mixing behaviour [1]. The two-equation models such as the variations of the k-ϵ and k-ω greatly overestimated the vertical velocity below the mixing. The mixing location fluctuated along the ceiling and produced weaker time-averaged velocities in measurements in a test facility. With RANS models the mixing location remained stationary. In our earlier large-eddy simulations the jet mixing location was too unstable and one jet pushed the other away. The jets are quite close to each other and turbulence formation ahead of the mixing was weak. If the jets were turbulent the mixing would likely be enchanced.

In this work artificial velocity perturbations have been applied to start up the turbulence. Evaluations have been done between different turbulence models such as the dynamic Smagorinsky and the dynamic kinetic energy equation models. The influence of discretization choices of the convective term to the flow has also been studied. In the computations we have relied on the OpenFOAM-1.5 finite volume code [12]. The computations have been done in parallel. The cost of doing LES is today within the reach in practical indoor ventilation applications, but in order to get improvement over RANS the modelling of LES must be done carefully.

2 Simulation Model

The model consists of an office room where two ventilation beams are embedded asymmetrically on the roof. Air temperature is constant 20°C in this case. The beams are modelled with large boxes, where the long sides are velocity inlets for the simulation domain (Fig. 1). The problem setup was brought up by Turku regional office of Finnish Institute of Occupational Health (FIOH). They have also made the measurements of a free jet with one beam and the mixing jets with two beams in a full scale test room, which was created for this problem. The box model originates from RANS ventilation modelling, where it is an established procedure to fix the velocity and turbulence values in a chosen plane section. Here the mean inlet velocity depends on the z-coordinate and the peak of 0.65 m/s lies 0.025 m below the roof. Recirculation air outlets are on the box bottoms and the mass flow is controlled by pressure. A fixed pressure outlet is on the back wall for air removal.

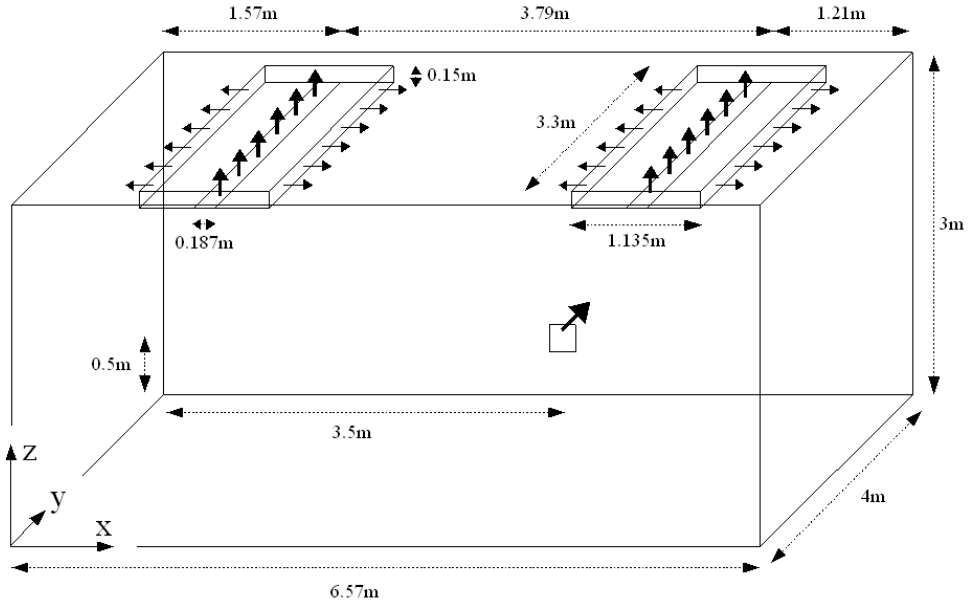

Fig. 1: Simulation domain. The ventilation beams are modelled with boxes. The beams are located in asymmetric distances from the end walls. Mixing of the two jets in the middle is under most interest.

3 Governing equations

In large-eddy simulation small scale turbulence is modelled and large scale flow is resolved. A large scale variable can be described with a linear filtering function from the local variable

$$\widehat{f}(x,t) = \int_V G(|x-x'|) f(x',t) dx'. \tag{1}$$

G is a weighing factor and filtered variables are denoted with the tophat $\hat{\theta}$. Most often grid filtering is used as the filtering operation. A cell value is considered to be the local average around the cell centre. Here a geometrical filter width is considered $\Delta = \sqrt[3]{\Delta_1\Delta_2\Delta_3}$, where the components are cell dimensions. Grid filtering does not satisfy the commutation assumption required from the filter, but computationally this should be more efficient for achieving certain accuracy than using a specific filter and finer grid [5, pp. 12-14].

Incompressible Navier-Stokes equations with the filtered variables in the conservation form are

$$\frac{\partial \hat{u}_i}{\partial t} + \frac{\partial \hat{u}_i \hat{u}_j}{\partial x_j} = -\frac{1}{\rho}\frac{\partial \hat{p}}{\partial x_i} + \frac{\partial}{\partial x_j} 2\nu D^*_{ij} - \frac{\partial \tau_{ij}}{\partial x_j} \tag{2}$$

$$\frac{\partial \hat{u}_j}{\partial x_j} = 0, \tag{3}$$

where the subgrid-scale stress tensor is

$$\tau_{ij} = \widehat{u_i u_j} - \hat{u}_i \hat{u}_j. \tag{4}$$

In the remaining text the top hats of the large scale variables will be left away to save effort and to avoid too many different marks over the variables. The strain rate tensor and its deviatoric form are

$$D_{ij} = \frac{1}{2}\left(\frac{\partial u_i}{\partial x_j} + \frac{\partial u_j}{\partial x_i}\right) \tag{5}$$

$$D^*_{ij} = D_{ij} - \frac{1}{3} D_{kk}. \tag{6}$$

Eqs. (2) could be simplified with the incompressibility condition (3) but for numerical reasons this is not done in OpenFOAM.

The passive scalar transport equation is

$$\frac{\partial \theta}{\partial t} + \frac{\partial \theta u_j}{\partial x_j} = \frac{\partial}{\partial x_j}\left(\alpha \frac{\partial \theta}{\partial x_j}\right) + \frac{\partial q_j}{\partial x_j}, \tag{7}$$

where α is the diffusion coefficient and q_j is the turbulent flux of the transportant θ

$$q_j = -\frac{\nu_{sgs}}{Sc_t}\frac{\partial \theta}{\partial x_j}, \tag{8}$$

where Sc_t is the turbulent Schmidt number.

4 Turbulence models

The subgrid-scale stresses of Eq. (4) are modelled with the general eddy viscosity model

$$\tau_{ij} = \frac{2}{3} k_{sgs}\delta_{ij} - 2\nu_{sgs} D^*_{ij}. \tag{9}$$

This follows from the Boussinesq approximation

$$\tau_{ij} - \frac{1}{3}\tau_{kk}\delta_{ij} = 2\nu_{sgs}D^*_{ij}, \tag{10}$$

which relates the subgrid-scale stresses to the resolved strain rate velocity and the eddy viscosity ν_{sgs}. The effect of trace terms is assumed isotropic and it is connected with the pressure.

4.1 Dynamic Smagorinsky

In Smagorinsky type models the eddy viscosity and the subgrid-scale turbulence kinetic energy are calculated explicitly from the strain rate velocity

$$\begin{aligned} \nu_{sgs} &= C_D\Delta^2||D|| &(11)\\ k_{sgs} &= C_I\Delta^2||D||^2. &(12)\end{aligned}$$

In the dynamic Smagorinsky model also coefficients C_D and C_I are computed from the resolved field. Test filter $\widetilde{f}$ is formally defined as the sub-grid scale filter 1. In this work a test filter which takes surface average of the resolved variable from the cell faces is applied. The filter width becomes $\widetilde{\Delta} = 2\Delta$. The coefficients are obtained with the assumption that they remain constant from grid to test scales. The subgrid-scale stresses $\tau_{ij} = \breve{u}_i\breve{u}_j - \breve{\widehat{u}}_i\breve{\widehat{u}}_j$ and the subtest-scale stresses $T_{ij} = \widetilde{\breve{u}_i\breve{u}_j} - \breve{\widetilde{u}}_i\breve{\widetilde{u}}_j$ form a relationship with the resolved stresses L_{ij}

$$\begin{aligned} L_{ij} &= \widetilde{u_iu_j} - \widetilde{u}_i\widetilde{u}_j\\ &= T_{ij} - \widetilde{\tau}_{ij}. &(13)\end{aligned}$$

The subgrid- and subtest-scale stresses are parametrized and substituted into (13)

$$\begin{aligned} \tau^*_{ij} &= -C_D\Delta^2||D||D^*_{ij} = -C_DB_{ij} &(14)\\ T^*_{ij} &= -C_D\widetilde{\Delta}^2||\widetilde{D}||\widetilde{D}^*_{ij} = -C_DA_{ij} &(15)\\ L^*_{ij} &= -C_D\left(A_{ij} - \widetilde{B}_{ij}\right) &(16)\end{aligned}$$

Coefficient C_D is solved with the least squares method and becomes

$$C_D = -\frac{\left\langle L^*_{ij}, \left(A_{ij} - \widetilde{B}_{ij}\right)\right\rangle}{\left\langle \left(A_{mn} - \widetilde{B}_{mn}\right), \left(A_{mn} - \widetilde{B}_{mn}\right)\right\rangle}, \tag{17}$$

where the brackets $\langle\ \rangle$ denote spatial average over the simulation domain and

$$L_{ij} = \widetilde{u_iu_j} - \widetilde{u}_i\widetilde{u}_j \tag{18}$$

[6, 7, 12]. Coefficient C_I is solved similarly

$$C_I(t) = \frac{\left\langle k, \left(a - \widetilde{b}\right)\right\rangle}{\left\langle \left(a - \widetilde{b}\right), \left(a - \widetilde{b}\right)\right\rangle}, \tag{19}$$

where

$$k = \frac{1}{2}\left(\widetilde{u_k u_k} - \widetilde{u}_k \widetilde{u}_k\right). \quad (20)$$

$$a = \widetilde{\Delta}^2 ||\widetilde{D}||^2 \quad (21)$$

$$b = \Delta^2 ||D||^2. \quad (22)$$

4.2 Localized dynamic Smagorinsky

In the localized version of the dynamic Smagorinsky model the model coefficients are only local averages, instead of finding a global constant or an average in some particular direction. This leads to stability problems, which can be avoided deriving the coefficients iteratively instead of the least squares method. The Smagorinsky coefficient is

$$C_D = \frac{\left(L^*_{ij} - \widetilde{C^0_D B_{ij}}\right) A_{ij}}{A_{mn} A_{mn}}, \quad (23)$$

where coefficient C^0_D is from the preceding time step [3]. Large negative coefficients also need to be handled for stability reasons. Here the negative values are simply cut off so that the subgrid-scale viscosity is always non-negative. This means that kinetic energy is not transferred from the sub-grid scales to the larger scales. The coefficient C_I is iterated likewise

$$C_I(t) = \frac{\left(k - \widetilde{C^0_I b}\right) a}{a^2}. \quad (24)$$

4.3 Dynamic turbulence kinetic energy equation

In this model a transport equation for subgrid scale turbulence kinetic energy is solved

$$\frac{\partial k_{sgs}}{\partial t} + \frac{\partial k_{sgs} u_j}{\partial x_j} = -2\tau_{ij}||D||^2 - C_\epsilon \frac{k^{3/2}_{sgs}}{\Delta} + \frac{\partial}{\partial x_j}\left(\nu_{eff}\frac{\partial k_{sgs}}{\partial x_j}\right) \quad (25)$$

[12]. The turbulent eddy-viscosity depends on the turbulence kinetic energy, local length scale and dynamic coefficient C_k.

$$\nu_{sgs} = C_k \Delta \sqrt{k_{sgs}}. \quad (26)$$

The coefficient C_k is

$$C_k = -\frac{\left\langle L^*_{ij}, MM \right\rangle}{\langle MM, MM \rangle}, \quad (27)$$

where

$$L_{ij} = \widetilde{u_i u_j} - \widetilde{u}_i \widetilde{u}_j \quad (28)$$

$$MM = \Delta(\sqrt{\widetilde{k_{sgs}}} D - 2\sqrt{k + \widetilde{k}_{sgs}}\widetilde{D}) \quad (29)$$

The coefficient C_ϵ is

$$C_\epsilon = \frac{\langle e, mm \rangle}{\langle mm, mm \rangle}, \tag{30}$$

where

$$e = 2\Delta C_k \left(\sqrt{\widetilde{k_{sgs}}} ||D||^2 - 2\sqrt{k + \widetilde{k}_{sgs}} ||\widetilde{D}||^2 \right) \tag{31}$$

$$mm = \frac{1}{2\Delta} \left(k + \widetilde{k}_{sgs} \right)^{3/2} - \frac{1}{\Delta} \widetilde{k}_{sgs}^{3/2}. \tag{32}$$

4.4 Spalart-Allmaras

The Spalart-Allmaras model is a one-equation turbulence model, which was originally developed for RANS simulations. With some modifications it has been developed for detached-eddy simulations (DES), which should combine the worlds of LES and RANS. With the approach the attached boundary layers are ideally simulated in RANS mode and rest of the flow in LES mode, where the Spalart-Allmaras model should work like Smagorinsky type models. The trick is turbulence length scale

$$\tilde{d} = \min \left(C_{DES} \Delta, d \right), \tag{33}$$

where d is the distance from cell centre to closest wall and Δ is the largest dimension of concerned cell. The turbulent eddy-viscosity is

$$\nu_{sgs} = \tilde{\nu} f_{v1}, \tag{34}$$

where $\tilde{\nu}$ is viscosity-like variable which is solved from transport equation

$$\begin{aligned} \frac{\partial \tilde{\nu}}{\partial t} + \frac{\partial \tilde{\nu} u_j}{\partial x_j} &= \frac{1}{\sigma} \left[\frac{\partial}{\partial x_j} \left[(\nu + \tilde{\nu}) \frac{\partial \tilde{\nu}}{\partial x_j} \right] + ||C_{b2} \nabla \tilde{\nu}||^2 \right] \\ &\quad + C_{b1} \tilde{S} \tilde{\nu} - C_{w1} f_w \frac{\tilde{\nu}^2}{\tilde{d}^2} \end{aligned} \tag{35}$$

[8, 12]. The missing variables and functios are

$$\begin{aligned} \tilde{S} &= f_{v3} S + f_{v2} \frac{\tilde{\nu}}{\kappa^2 \tilde{d}^2} \\ S &= \sqrt{2 \Omega_{ij} \Omega_{ij}} \\ \Omega_{ij} &= \frac{1}{2} \left(\frac{\partial u_i}{\partial x_j} - \frac{\partial u_j}{\partial x_i} \right) \\ f_{v1} &= \frac{\chi^3}{\chi^3 + C_{v1}^3} \\ f_{v2} &= \frac{1}{(1 + \chi / C_{v2})^3} \\ f_{v3} &= \frac{(1 + \chi f_{v1})[3(1 + \chi/C_{v2}) + (\chi/C_{v2})^2]}{C_{v2}(1 + \chi/C_{v2})^3} \end{aligned}$$

$$
\begin{aligned}
f_w &= g\left[\frac{1.0+C_{w3}^6}{g^6+C_{w3}^6}\right]^{1/6} \\
\chi &= \frac{\tilde{\nu}}{\nu} \\
g &= r + C_{w2}\left(r^6 - r\right) \\
r &= \frac{\tilde{\nu}}{\tilde{S}\kappa^2\tilde{d}^2}.
\end{aligned}
$$

The missing constants are given in table 1.

Table. 1: Spalart-Allmaras model coefficients

$C_{DES} = 0.65$	$C_{b1} = 0.1355$	$C_{w2} = 0.3$	$C_{v1} = 7.1$
$\sigma = 2/3$	$C_{b2} = 0.622$	$C_{w3} = 2.0$	$C_{v2} = 5.0$

5 Numerical algorithm

The simulations are done using the oodles-solver of the finite-volume code OpenFOAM 1.5. The incompressible solver employs the PISO pressure correction algorithm [pressure implicit with splitting of operators]. The important steps of the algorithm are described in table 2.

Table. 2: The applied PISO algorithm

1. Momentum equations are defined
2. Momentum predictor is performed
3. Intermediate velocities are solved
4. Face fluxes are calculated
5. Pressure equation is solved
6. Velocities are corrected
7. Boundary conditions are updated
8. Repeat from 3.
9. Start new time step from 1.

The conservative form of the momentum equations (2) can be written in a finite volume form and discretized by using Gauss theorem as

$$
\frac{\partial}{\partial t}\int_{V_p} u dV = -\int_{V_p} \nabla\cdot(u^T u)dV + \int_{V_p}\nabla\cdot\nu_{eff}\nabla u - \int_{S_p}\frac{1}{\rho}p dS \tag{36}
$$

$$
\begin{aligned}
V_c\frac{\partial u}{\partial t} &= \sum_f \phi u S_f + \sum_f \nu_{eff}(\nabla\phi)_f S_f - \sum_f p_f S_f \\
&= R(u) - \sum_f p_f S_f
\end{aligned} \tag{37}
$$

Velocities in the convective term of the momentum equation are split between face flux ϕ and cell velocity u to linearize the equations for velocity. Despite of the collocated grid, the algorithm produces an oscillation free pressure field without explicit Rhie-Chow correction term [4]. The set of linearized discrete equations can be written in algebraic form as follows

$$Au = H - \nabla p \tag{38}$$

Initial velocity guess is done by solving the momentum equations with an old pressure field

$$u = \frac{1}{A}H - \frac{1}{A}\nabla p \tag{39}$$

The step is called momentum-predictor and it is used to update the coefficients of A and H. It is not necessary for the convergence but it could be beneficial. Pressure correction loop begins after this. The intermediate velocities are calculated from equation

$$u^* = \frac{1}{A}H \tag{40}$$

the pressure term being neglected. New face fluxes are calculated, but the continuity equation is not satisfied yet. Pressure equation is obtained from

$$u = u^* - \frac{1}{A}\nabla p \tag{41}$$

by taking divergence and applying the continuity equation $\nabla \cdot u = 0$

$$\nabla \cdot u^* = \nabla \cdot \frac{1}{A}\nabla p \tag{42}$$

In the above equation face fluxes ϕ^* are used instead of u^* to solve the pressure. The pressure gradient is considered on the cell faces and cell values are obtained for the pressure. Face fluxes and velocities are then corrected

$$u = u^* - \frac{1}{A}\nabla p \tag{43}$$

The coefficients of the linearized momentum equation (38) are updated and the pressure correction procedure is repeated to improve convergence and mass balance, before solving the passive scalar transport equation and moving to the next time step. More detailed description of the pressure correction algorithm is found in [4]

For time integration the implicit second order accurate backward scheme has been applied

$$u^*_{n+1} = u_n + \left(\frac{3}{2}R(u)_{n+1} - R(u) + \frac{1}{2}R(u)_{n+1}\right). \tag{44}$$

Crank-Nicholson scheme would be more accurate, but it was much slower and convergence problems were experienced.

The Laplacian term of equation (36) is discretizated with surface integrals in second order accuracy. Surface gradients are calculated with linear differencing between cell center values. The discretization is implicit with orthogonal meshes [11].

In this work more interest is placed in the convective term, how the cell velocities are interpolated in order to obtain the convective fluxes. Using a linear face interpolation for the velocities corresponds to second-order central differencing. A limited scheme called limitedLinearV was applied in the previous simulations. It is a total variational diminishing method, which added quite a lot numerical diffusion even on the parameter value for most accuracy. In OpenFOAM there is a scheme called filteredLinear, which is aimed at maintaining required accuracy while removing high freguency oscillations. These oscillations could happen with the central differencing scheme if there is not enough dissipation in the flow. The filtering is done by comparing face fluxes and introducing small amounts of upwinding. FilteredLinear2V is a similar scheme, but the filtering can be adjusted by two parameters.

6 Results

Seven simulations are included in this work, which are overviewed in Table 3. Comparisons have been done with different turbulence models and different discretization schemes of the convective term. The turbulence model formulations have been presented in section 4 and discretization schemes have been explained shortly in 5.

Table. 3: Simulation setup choices of the reported simulations

Simulation	1	2	3	4	5	6	7
Turb. model	dyn. Smag.	dyn. Smag.	dyn. Smag.	loc. dyn. Smag	dyn. TKE	dyn. TKE	Spalart-Allmaras
Conv. scheme	limit.	linear	filt.2	filt.2	filt.2	filt.1	filt.2

6.1 Coumputational grid

The Kolmogorov length scale, where the viscous dissipation takes place, is in this case approximately

$$\Delta = \left(\nu^3 \delta / U^3\right)^{1/4} = 0.2 \text{ mm} \tag{45}$$

[2, pp. 400]. Above δ is the boundary-layer height and U the free stream velocity. The length scale shows that an accurate direct numerical simulation would reguire a very fine grid. Large-eddy simulation allows a use of much coarser grids, but the grid should still be fine enough to capture the eddies of relevant scales in the problem.

Near walls the flow structures have a length scale

$$\Delta_w = \nu\sqrt{\rho/\tau_w}, \tag{46}$$

where the wall shear stress is

$$\tau_w = \rho\nu\frac{\partial\overline{u}}{\partial y}. \tag{47}$$

When solving the flow accurately near the wall with LES it would be desirable to obtain the length scale $y^+ = 1$ in the wall normal direction to [5, pp. 76]. In present simulation this was only done on the ceiling. On the left and right walls $y^+ \approx 10$ and on the other walls $y^+ \approx 20$. Boundary layer regions are refined with geometrical ratio 1.1. For all simulations the same orthogonal structured grid has been used, which consists of 3.5 million cells (Fig. 2). The extreme grid cell dimensions are shown in Table 4. On the horizontal jet regions the grid density is $\Delta y = 5$ cm in a streamwise direction and $\Delta y = 2$ cm in a transverse direction. The maximum Courant number remained below 4 in the simulations when using a time step $\Delta t = 0.005$ s.

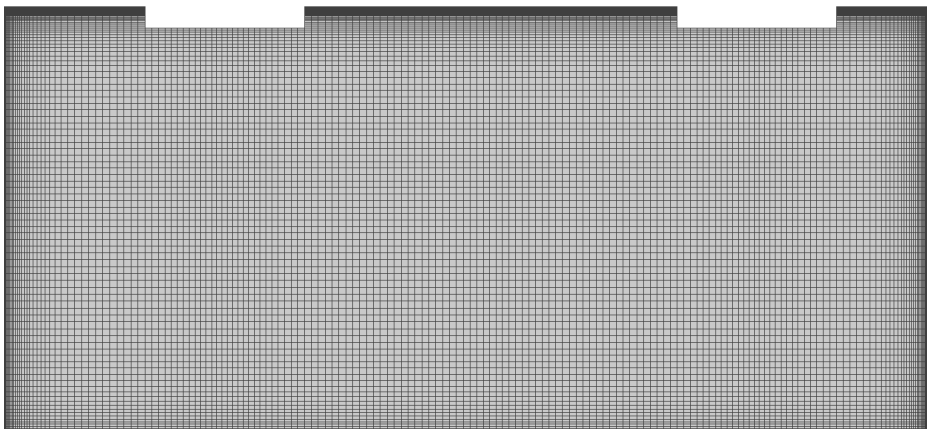

Fig. 2: Intersection of the computational grid.

Table. 4: Minimum and maximum cell dimensions in the grid.

Δ_x^{wall}	Δ_x^{max}	Δ_y^{wall}	Δ_y^{max}	Δ_z^{roof}	Δ_z^{floor}	Δ_z^{max}
5 mm	5 cm	1 cm	2 cm	0.6 mm	1.5 cm	5 cm

6.2 Boundary Conditions

A zero gradient in a surface normal direction has been used for the pressure on all boundaries apart from the outlets, where the pressure is fixed. On the

recirculation outlets the pressure is self-adjusted to keep mass flux close to the target value

$$\delta p_{out1} = constant \cdot (\dot{m}_{out1} - \dot{m}_{target}) \tag{48}$$

A zero slip condition is used for velocity on the walls. On the outlets the velocity gradient in the normal direction is set to zero. In earlier large-eddy simulations the inlet condition was a fixed velocity profile $U_{in}(z)$ (Fig. 3). Based on the free jet measurements the profile is not laterally completely uniform, but in the simulations the profile is based on centerline measurement. Without turbulence the jets attatched to the wall and did not spread out like they should. This was thought to contribute to the instability of the jet mixing location.

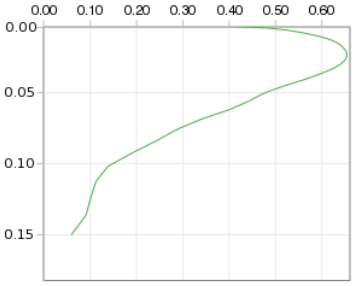

Fig. 3: Fixed turbulent velocity profile $U_{in}(z)$ for the inlets.

In the present work random inlet velocity fluctuations are adopted in order to enchance the start up of turbulence. Let X_i be a random variable with a uniform distribution between an interwall $[-0.5 \ldots 0.5]$. On each time step for each boundary cell face the velocity is changed with formula

$$u_i^{n+1} = (1 - \alpha)u_i^n + \alpha C(\alpha) X_i I_i U_{in}, \tag{49}$$

where I_i is turbulence intensity, α adjusts the rate of fluctuation change and $C(\alpha)$ is a coefficient to fix the root mean square (RMS) velocity fluctuation u'_i when $\alpha \neq 1$. Here $\alpha = 0.2$. We have assumed the magnitude of RMS velocity fluctuation to be equal in each direction with a turbulence intensity 0.27. In reality there is more fluctuation in the streamwise direction and less against the wall, but only the streamwise RMS velocity fluctuation u'_1 has been measured. In our simulations the inlet disturbances indeed caused more rapid development of turbulence in the flow.

With the Smagorinsky turbulence models the sub-grid scale kinetic energy k_{sgs} and the eddy viscosity ν_{sgs} are explicitly calculated from the flow field and it is not possible to adjust the flow with boundary conditions. With the dynamic TKE model condition $k_{sgs} = 0$ was first applied for the SGS turbulence kinetic energy of the jets, but some fitting value has also been tried. Normal zero gradient condition was applied on the other boundaries. The value is near zero on the walls which is the physical condition.

In the Spalart-Allmaras turbulence model a viscosity-like variable $\tilde{\nu}$ is solved. The model will not start up when $\tilde{\nu} = 0$ on the inlets, so $\tilde{\nu} = 5\nu$ is applied instead. On the walls $\tilde{\nu} = 0$ is used.

6.3 Convective scheme comparisons

In the simulations 1, 2 and 3 the influence of the convective discretization choice has been investigated while using the dynamic Smagorinsky model. The limited scheme has a clear damping influence, since the velocity gradients are relatively smooth (Fig. A-4). The artificial velocity fluctuations are killed and turbulence originates later in the downstream (Fig. A-7). In the earlier simulations with the fixed inlet velocity boundary conditions one of the jets eventually pushed the other jet away. In this case the same phenomenom occurs with the outer edges of the jets. The jet velocity profile does not match the measurements either (Fig. 4) and the jet is least turbulent near the wall (Fig. 5). This scheme is not recommended in LES applications like this.

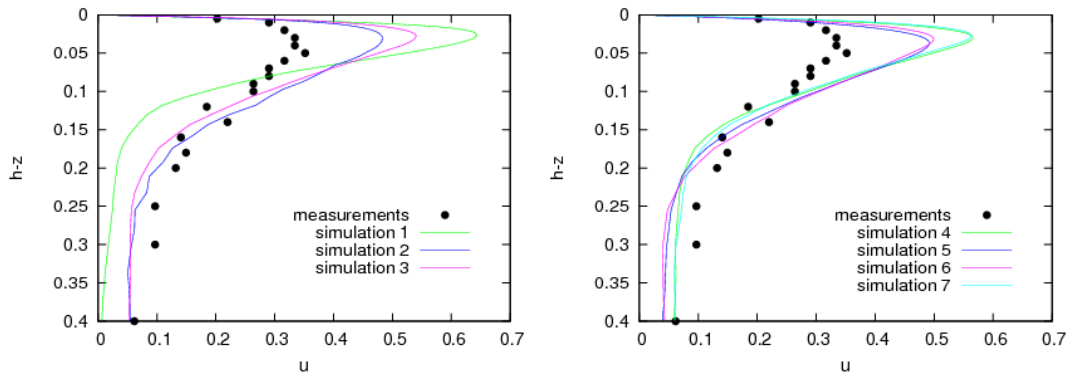

Fig. 4: The mean velocity $\overline{u}_x$ [m/s] at a distance of 0.7 m from the inlet. Simulation 1 results are from $y = 3$ m and the other results from $y = 2$ m. Measurements are from a single jet experiment.

In simulation 2 the central difference method is applied. The jets are mixing according to expections in the middle (Figs. A-14 and A-17). The velocity field looks more detailed with smaller turbulence scale. The velocity profile has come closer to the measurements, but the velocity is still too high (Fig. 4). The velocity field also looks unphysically oscillatory, which could explain the high level of turbulence (Fig. 5). The flow looks as if the velocity disturbances were transported along the flow, instead of the flow being genuinely turbulent. The mean velocity profile is not a perfectly smooth curve. It seems that more damping is needed or the grid should be improved.

The filtered schemes have a small stabilizing effect against the oscillations. In simulation 3 the second scheme has been used, which is more diffusive with the present parameter choices than the first alternative. The jet velocity has expectedly become higher (Fig. 4). Visually the flow field looks good, although

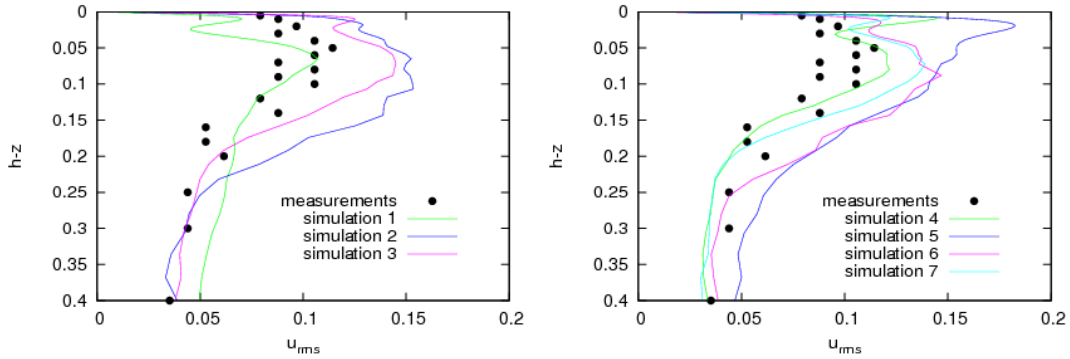

Fig. 5: The RMS velocity fluctuation $\sqrt{\overline{u_x' u_x'}}$ [m/s] at a distance of 0.7 m from the inlet. Simulation 1 results are from $y = 3$ m and the other results from $y = 2$ m. Measurements are from the single jet experiment.

the mean flow has not yet fully converged within the simulation time (Figs. A-24-A-28).

It is unclear how long it would take to achieve a fully converged result below the mixing jets. Sometimes the flow can stay in a certain state for a long period of time until finding a different state. This makes it impossible to compare the downflow velocity profiles precisely (Fig. 6). Generally these simulations give a vertical flow which is too narrow and too fast, but the results are closer to the measurements than RANS simulations in Ref. [1]. The real flow fluctuates more and spreads out with time.

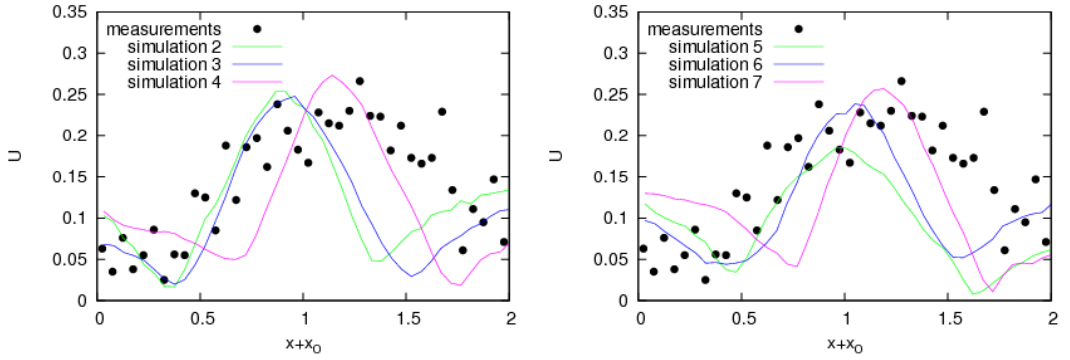

Fig. 6: The mean velocity $\overline{U}$ [m/s] below the mixing jets. Location is $x_0 = 2.5$ m, y = 2 m and z = 2 m.

6.4 Turbulence model comparisons

Comparisons have been made between the turbulence models described in Section 4. First simulations are done with the dynamic Smagorinsky model,

which appears to have insignificant influence to the flow. The turbulent eddy-viscosity is one decade below the laminar viscosity (Fig. A-33). Reason for this can be found from the Smagorinsky coefficient which is averaged over the simulation domain. In many places the coefficient is negative and the global coefficient ends up to a small value $cD = 0.00039$. In literature the Smagorinsky coefficient often has different formulation $C_s = \sqrt{cD} = 0.020$. There does not exist one correct value for the coefficient, but in several sources values around $C_s = 0.1 \ldots 0.2$ are mentioned. It would have been interesting to try the standard Smagorisnky model with different coefficients, but that was not accomplished. Instead a localized version of the dynamic model was implemented, and the results are in simulation 4. The turbulent viscosity range is clearly increased (Fig. A-47). This has somewhat reduced the jet velocity fluctuations which were too high (Fig. 5).

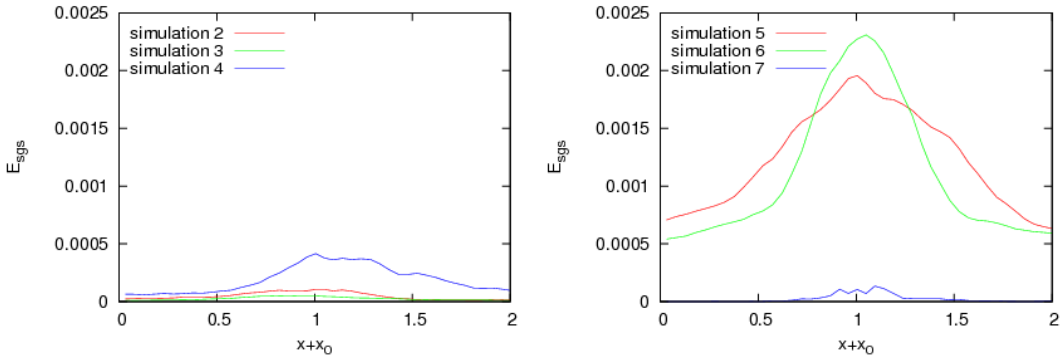

Fig. 7: The SGS turbulence kinetic energy $\overline{k}_{sgs}$ [m^2/s^2] below the mixing jets. Location is $x_0 = 2.5$ m, $y = 2$ m and $z = 2$ m.

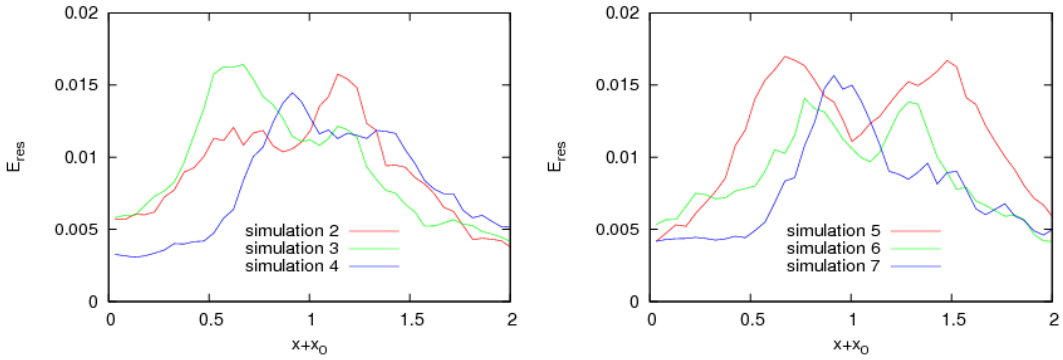

Fig. 8: The resolved turbulence kinetic energy $\frac{1}{2}\overline{u_k' u_{k'}}$ [m^2/s^2] below the mixing jets. Location is $x_0 = 2.5$ m, $y = 2$ m and $z = 2$ m.

Two simulations were done with the dynamic TKE equation model. In simulation 6 there was some SGS turbulence on the inlet and in simulation 5

not. The less dissipative filtered scheme was applied in simulation 6. With this turbulence model the jet mean velocity profiles became slightly closer to the measurements (Fig. 4). In simulation 5 the jet mixing location has moved partially away from the center (Fig. A-55). In simulation 6 the is higher turbulence viscosity near the wall and the velocity fluctuations are reduced. The flow field of simulation 6 looks good from all angles (Figs. A-66 and A-69). Certain LES models create often high eddy-viscosity values near the walls. This is undesirable and leads to wall friction errors. In simulations 5 and 6 high SGS stress peaks are seen near the wall (Fig. 9). Only with the localized dynamic Smagorinsky model that did not happen, because the model coefficient responds better to the local flow conditions and grid spacing.

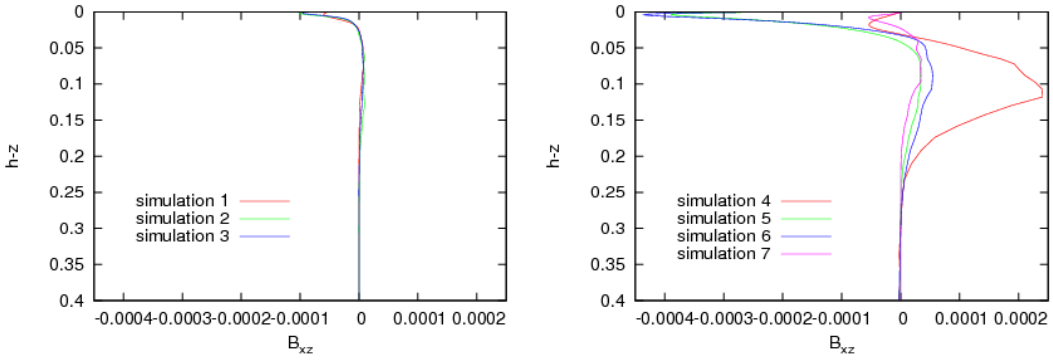

Fig. 9: The SGS stress $\overline{B}_{xz}$ [m^2/s^2] at a distance of 0.7 m from the inlet. Simulation 1 results are from $y = 3$ m and other results from $y = 2$ m.

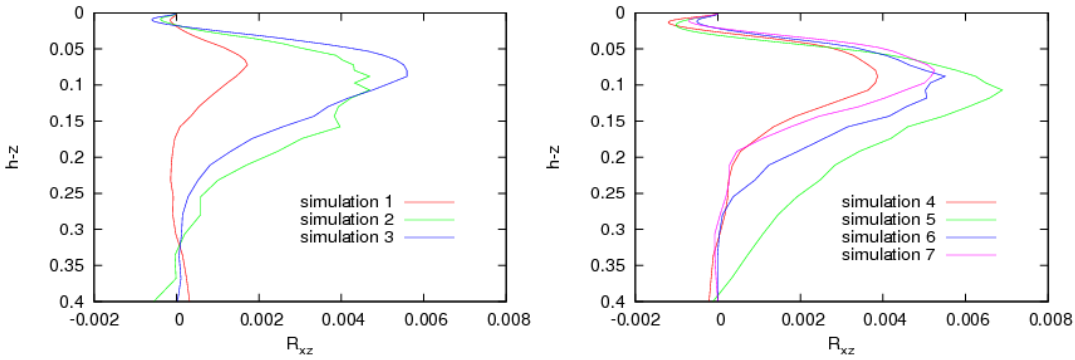

Fig. 10: The Reynolds stress $\overline{u_x' u_z'}$ [m^2/s^2] at a distance of 0.7 m from the inlet. Simulation 1 results are from $y = 3$ m and other results from $y = 2$ m.

In simulation 7 the Spalart-Allmaras DES model was applied. The flow field is very similar to the LES simulations (Figs. A-80 and A-81). It seems that the simultion did not turn into RANS mode in the boundary layers. The

turbulent viscosity does not have a high value near the wall and behaves time dependently everywhere (Fig. A-89). There is a probable reason for this. In the simulation we had $\Delta = \sqrt[3]{\Delta_1\Delta_2\Delta_3}$ instead of $\Delta = \max(\Delta_1\Delta_2\Delta_3)$ which leads to a thinner RANS layer. And the DES model itself has similar tendency on LES grids. Newer version of the model has targeted the issue [10].

The downward flow below the mixing jets is too focused with all turbulence models (Fig. 6). In simulation 4 the time averaged velocity peak is highest and the flow penetrates closest to the floor (Fig. A-55). In simulation 5 the velocity profile is the widest, but the flow state has changed more during the simulation time than in other cases (Fig. 8). The dynamic TKE model produced most SGS turbulence in the jet mixing (Fig. 7). Generally the model behaved well in these simulations, but a local dynamic model could be more accurate since the flow field is quite nonuniform. Such a model has been found reasonable for recirculating ventilation simulations [9]. Similar model is found in OpenFOAM as well.

7 Conclusions

In this work we have done isothermal large-eddy simulations of mixing planar jets in a ventilated room. Interest was placed on the mixing behaviour of the jets and improving the simulation of them. According to the measurements the jets should fluctuate and balance each other. We have struggled to reproduce the phenomenom properly in our simulations. It easily happens that one jet pushes the other jet away. This seems to happen particularly if the jets lack turbulence and the velocity profile does not spread enough. The jets are located quite near to each other and the conditions are not favourable for turbulence formation. Turbulence formation is improved by adding artificial velocity fluctuations to the inlets. The fluctuations improved stability between the jets, but the velocity and its variations remained incorrect.

Comparisons have been made between some convective term discretization schemes. Unphysical oscillations appeared in the velocity field with the 2nd order central difference. The grid is too coarse in some places which propably contributed to this phenomenom. With more dissipative schemes the problem dissappeared. However, too much dissipation rapidly dampens the velocity fluctuations, which in turn leads to imbalance between the jets. Different turbulence models were also compared. Influence of the turbulence model is small, but sometimes even small influence can make the flow behave differently. Each model have some different characteristics, but generally the dynamic TKE model behaved well for this application. The clear differences between the simulation and experimental results cannot be explained by turbulence models, since the difference in the results of different turbulence models were small.

The jet modelling strategy should be reconsidered to get more accurate results from large-eddy simulations. Either the boundary conditions could be

improved, or the jets could be simulated more accurately from the small scales and details which were not present in this model. This would easily lead to significant increase in computation time requirements.

8 Acknowledgement

This work was done as part of the Tekes-funded Flophy project. We would like to thank Turku regional office of FIOH for performing the full scale experimental measurements for validation of our simulation results. The project has also been supported by Halton Oy, Flakt Woods Oy and Olof Granlund Oy.

References

[1] Brockmann T., *Method of Large Eddy Simulation Applied to Recirculating Ventilation Flow in a Room*, Master's thesis, Department of Applied Mechanics, Espoo, 2009

[2] White F.M., *Viscous Fluid Flow*, McGraw-Hill, Singapore, 2006

[3] Piomelli U. and Liu J. *Large-eddy simulation of rotating channel flows using a localized dynamic model.* Physics of Fluids, Vol. 7, pp. 839-848, April 1995.

[4] Peng Krrholm F., *Rhie-Chow interpolation in OpenFOAM.* Appendix from *Numerical Modelling of Diesel Spray Injection and Turbulence Interaction*, Department of Applied Mechanics, Chalmers University of Technology, Gteborg, 2006

[5] Majander P., *Developments in Large Eddy Simulation*, Report 128, Laboratory of Applied Thermodynamics, Helsinki University of Technology, Espoo, 2000

[6] Germano.M, Piomelli U., Moin P., and Cabot W.H., *Large Eddy Simulation: A Dynamic Subgrid-scale Eddy Viscosity Model*, Physics of Fluids, Vol. 7, pp-1760-1765, 1991.

[7] Lilly D.K., *A Proposed Modification of the Germano Subgrid-scale Closure Method*, Physics of Fluids, Vol. 4, pp.633-635, 1992.

[8] Spalart P. R., Jou W.-H., Stretlets M. and Allmaras S. R., *Comments on the Feasibility of LES for Wings, and on a Hybrid RANS/LES Approach*, Advances in DNS/LES, Greyden Press, 1998

[9] Davidson L., *Large Eddy Simulation: A Dynamic One-Equation Subgrid Model for Three-Dimensional Recirculating Flow*, 11th Int. Symp. on Turbulent Shear Flow, Vol. 3, pp. 26.1-26.6, Grenoble, Sept. 8-11, 1997.

[10] Spalart P.R., Deck S., Shur M.L., Squires K.D., Strelets M.K., Travin A., *A New Version of Detatched-eddy Simulation, Resistant to Ambiguous Grid Densities*, Theor. Comput. Fluid Dyn. Vol. 20, pp. 181-195, 2006.

[11] *OpenFOAM 1.5 Programmers Guide*, OpenCFD, 2008.

[12] *OpenFOAM 1.5 source code*, OpenCFD, 2008.

A Room ventilation field images

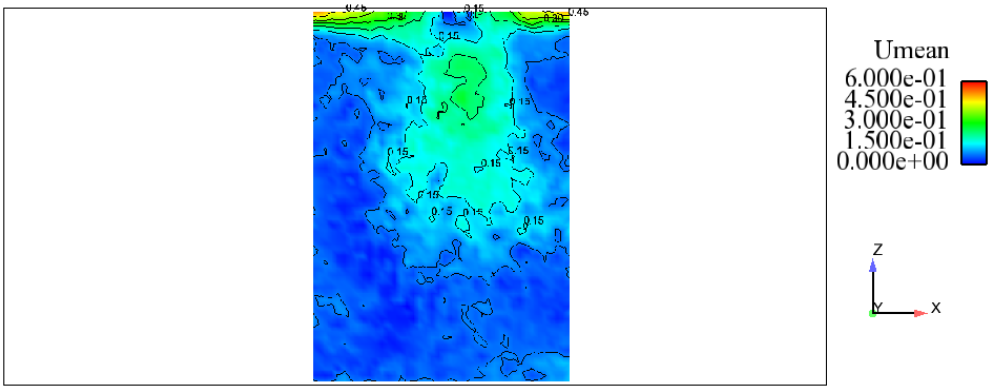

Fig. A-1: Experimental measurements. Velocity $\overline{u}$ [m/s] on plane $y = 2$ m. Measurement time 60 s per data point.

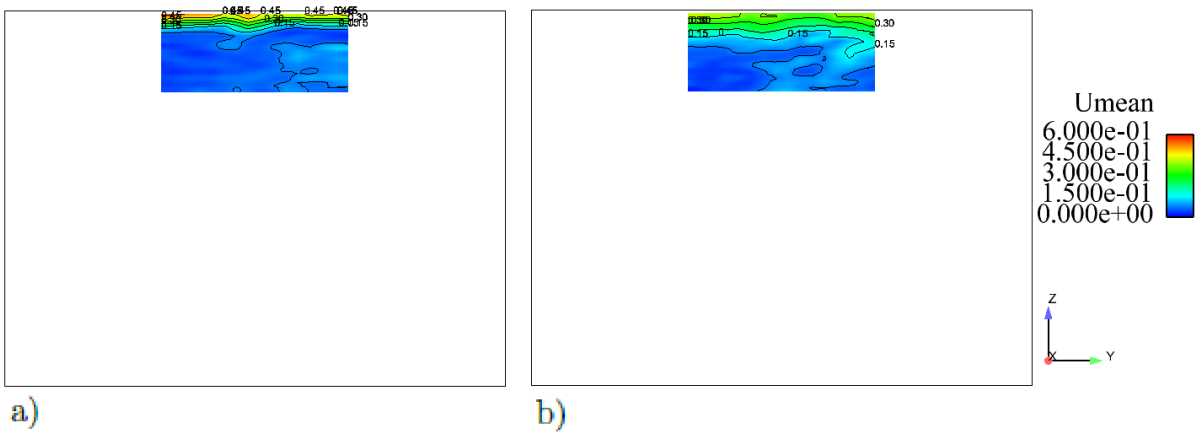

Fig. A-2: Experimental measurements. Velocity $\overline{u}$ [m/s] on plane a) $x = 2.5$ m b) $x = 3.0$ m. Measurement time 60 s per data point.

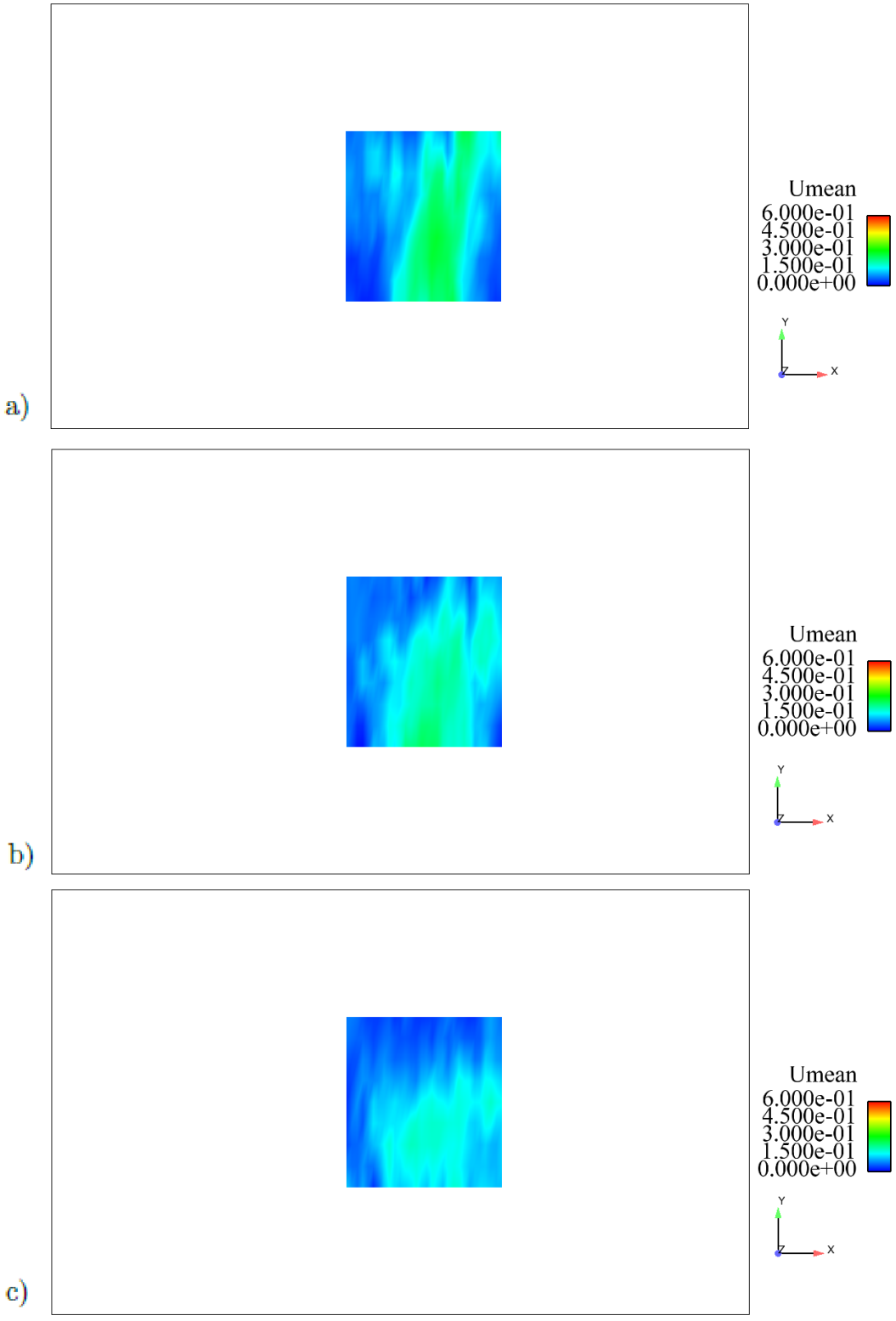

Fig. A-3: Experimental measurements. Velocity $\overline{u}$ [m/s] on plane a) $z = 2.5$ m b) $z = 2.0$ m c) $z = 1.5$ m. Measurement time 60 s per data point. a) b) c)

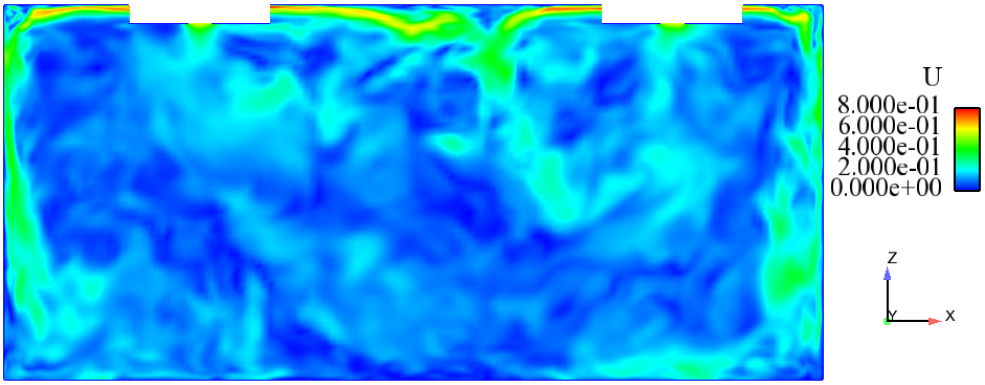

Fig. A-4: Simulation 1. Instantaneous velocity u [m/s] on plane $y = 2$ m.

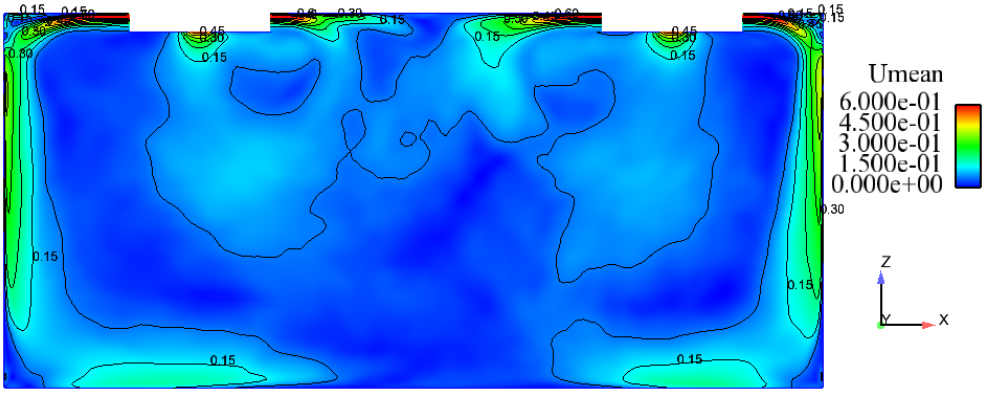

Fig. A-5: Simulation 1. Mean velocity $\overline{u}$ [m/s] on plane $y = 2$ m. Averaging time period 120 s.

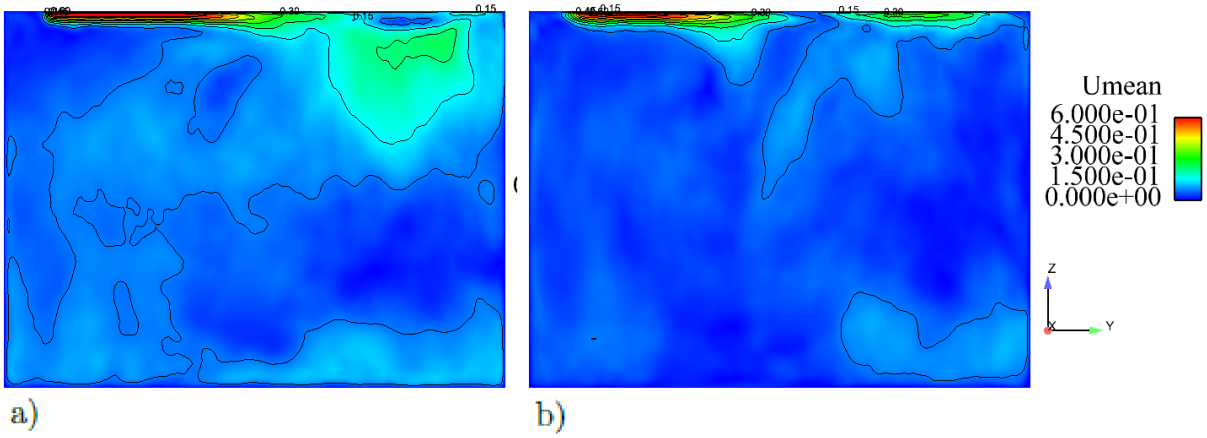

Fig. A-6: Simulation 1. Mean velocity $\overline{u}$ [m/s] on plane a) $x = 2.5$ m b) $x = 3.0$ m. Averaging time period 120 s.

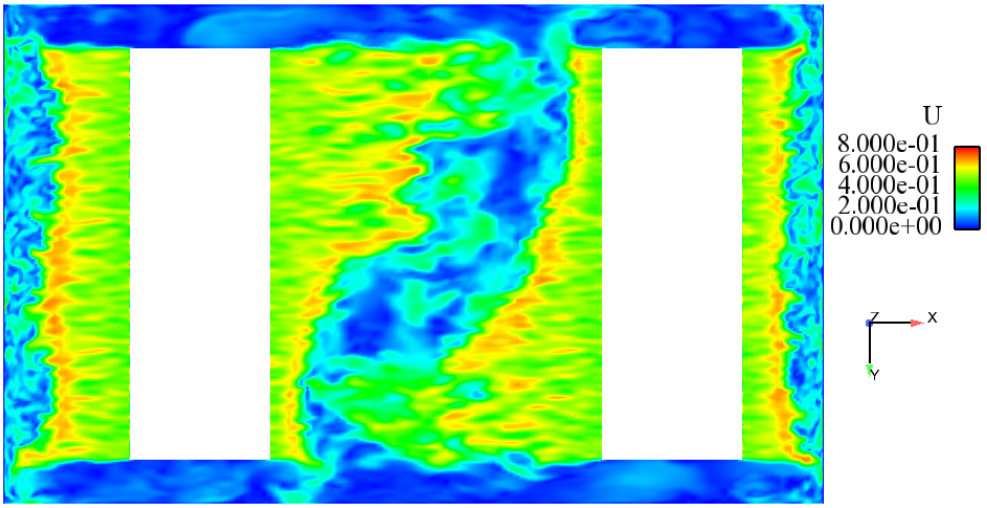

Fig. A-7: Simulation 1. Instantaneous velocity u [m/s] on plane $z = 2.95$ m.

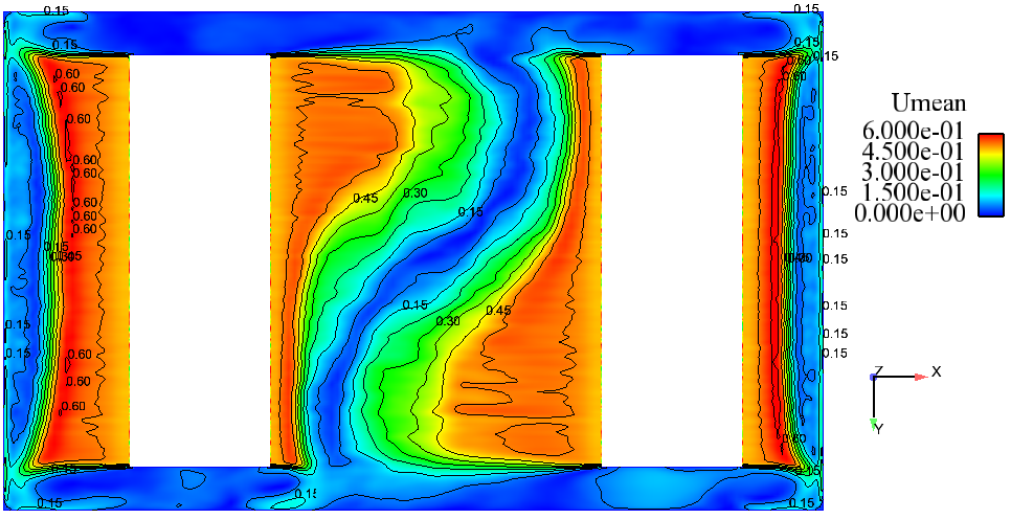

Fig. A-8: Simulation 1. Mean velocity $\overline{u}$ [m/s] on plane $z = 2.95$ m. Averaging time period 120 s.

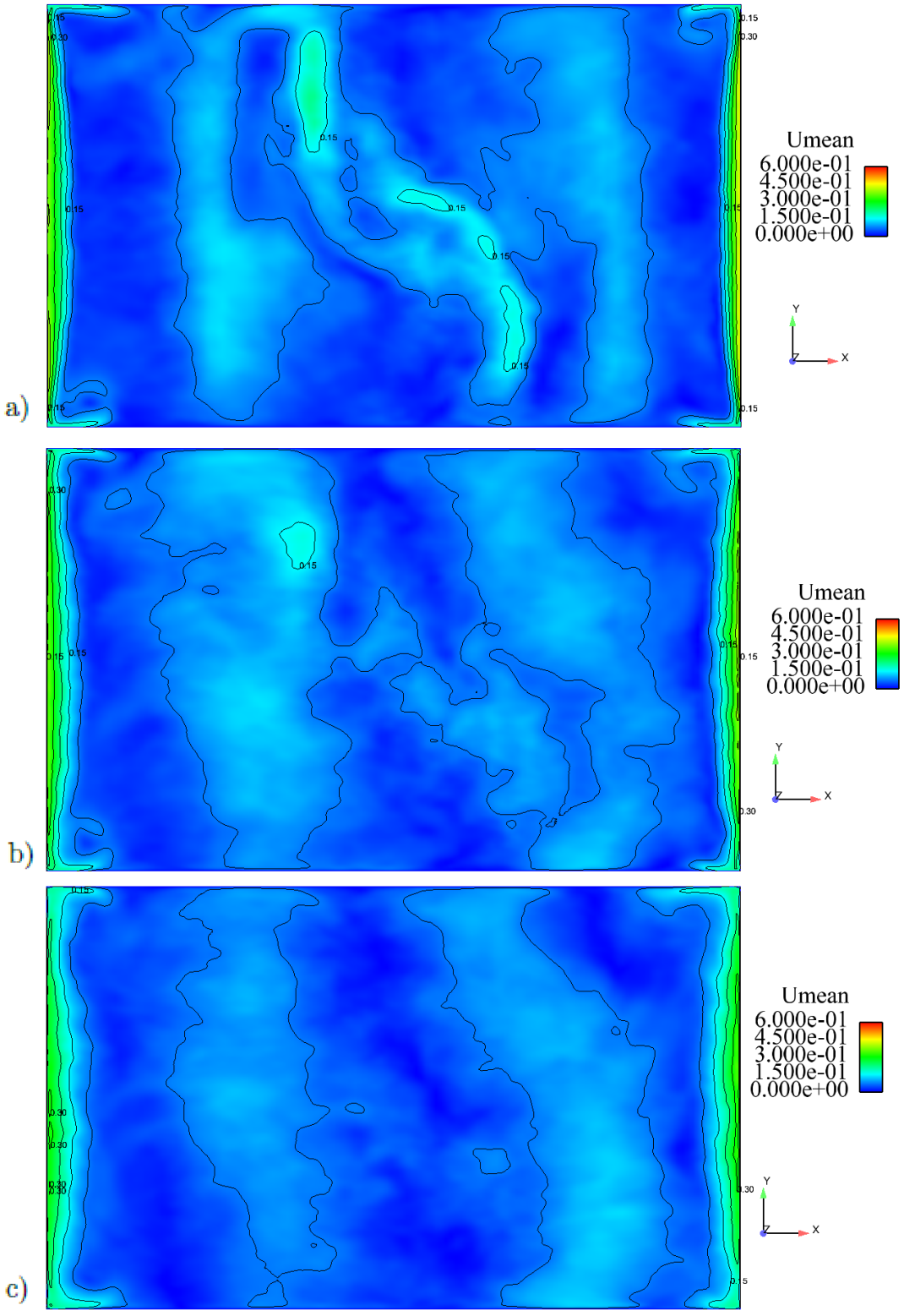

Fig. A-9: Simulation 1. Mean velocity $\overline{u}$ [m/s] on plane a) $z = 2.5$ m b) $z = 2.0$ m c) $z = 1.5$ m. Averaging time period 120 s.

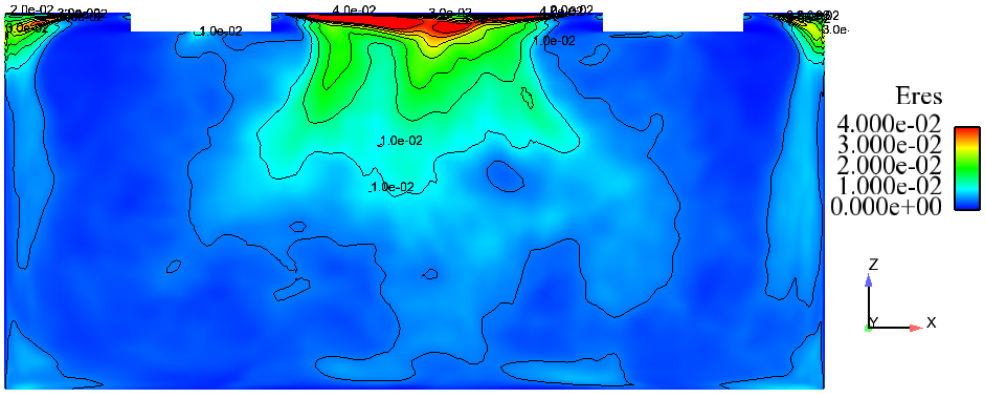

Fig. A-10: Simulation 1. Turbulence kinetic energy $\frac{1}{2}\overline{u'_k u'_k}$ [m^2/s^2] on plane $y = 2$ m. Averaging time period 120 s.

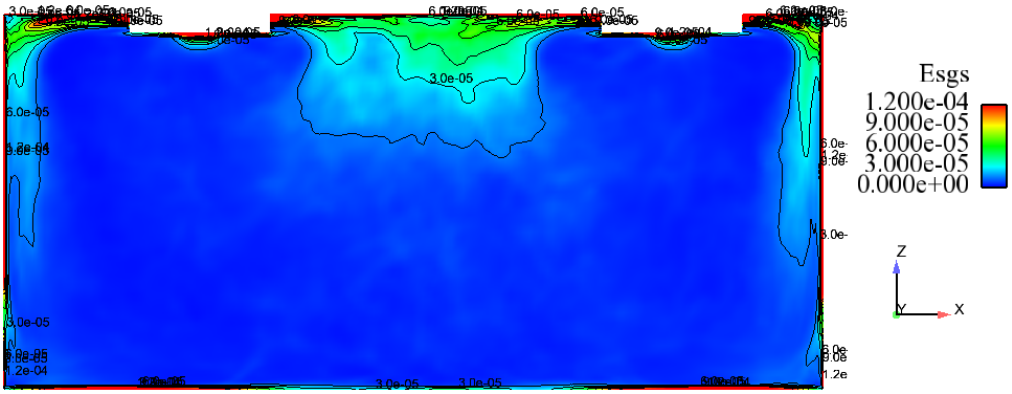

Fig. A-11: Simulation 1. Subgrid-scale turbulence kinetic energy e_{sgs} [m^2/s^2] on plane $y = 2$ m. Averaging time period 120 s.

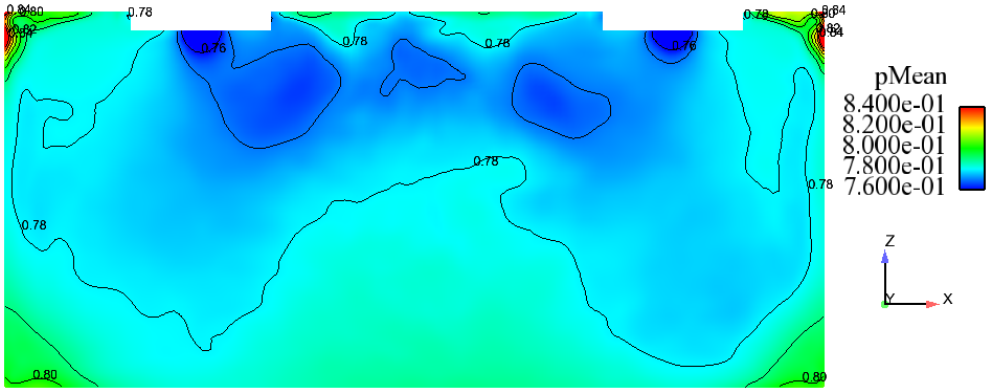

Fig. A-12: Simulation 1. Mean pressure $\overline{p}/\rho$ [m^2/s^2] on plane $y = 2$ m. Averaging time period 120 s.

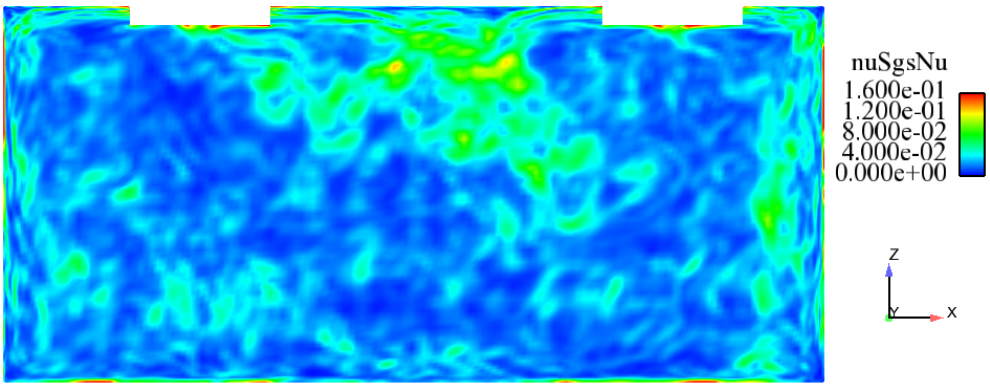

Fig. A-13: Simulation 1. Instantaneous eddy viscosity ν_{sgs}/ν on plane $y = 2$ m.

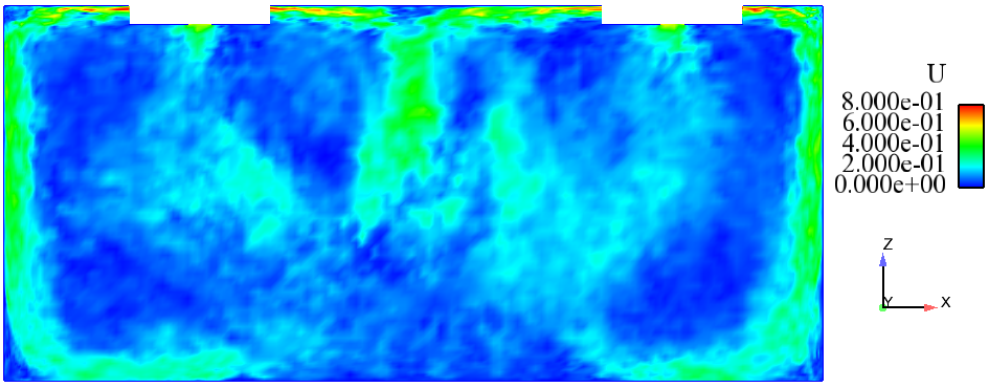

Fig. A-14: Simulation 2. Instantaneous velocity u [m/s] on plane $y = 2$ m.

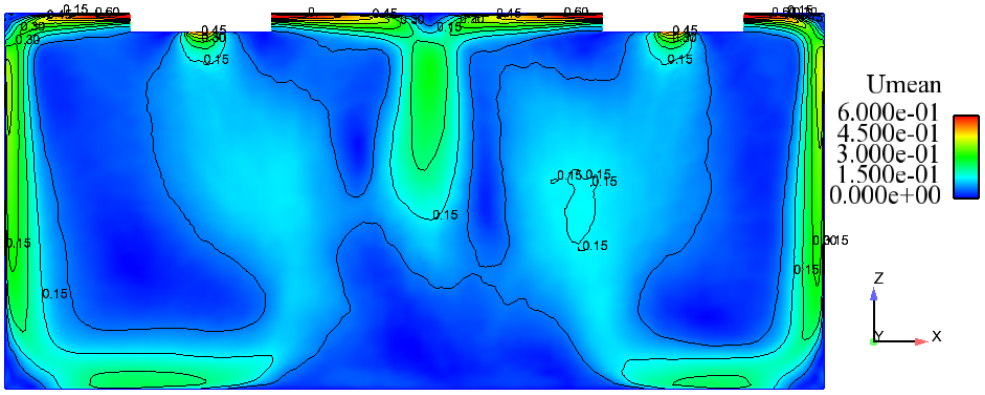

Fig. A-15: Simulation 2. Mean velocity $\overline{u}$ [m/s] on plane $y = 2$ m. Averaging time period 120 s.

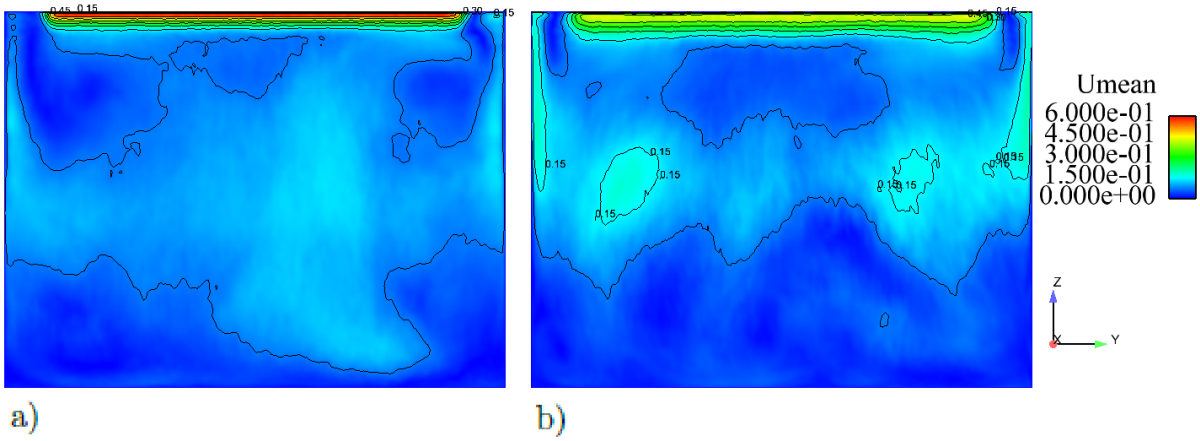

Fig. A-16: Simulation 2. Mean velocity $\overline{u}$ [m/s] on plane a) $x = 2.5$ m b) $x = 3.0$ m. Averaging time period 120 s.

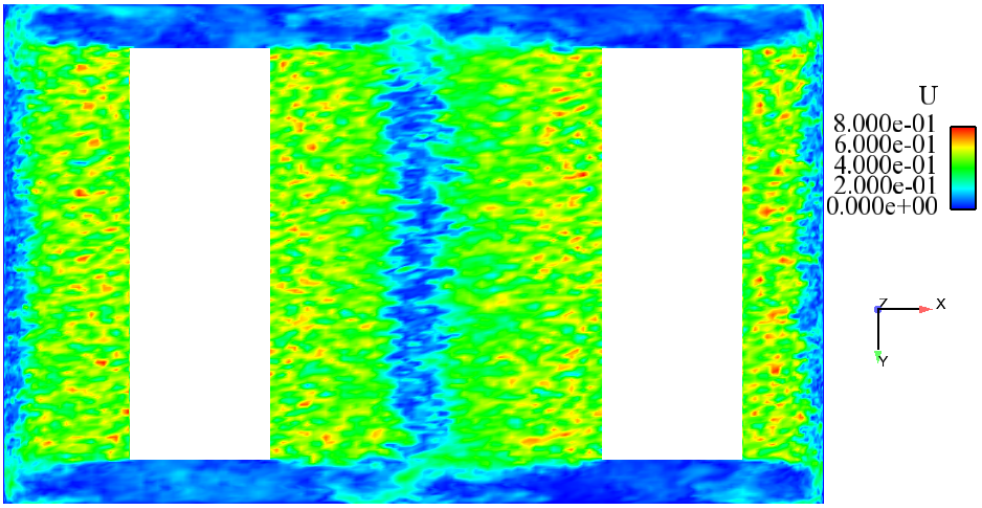

Fig. A-17: Simulation 2. Instantaneous velocity u [m/s] on plane $z = 2.95$ m.

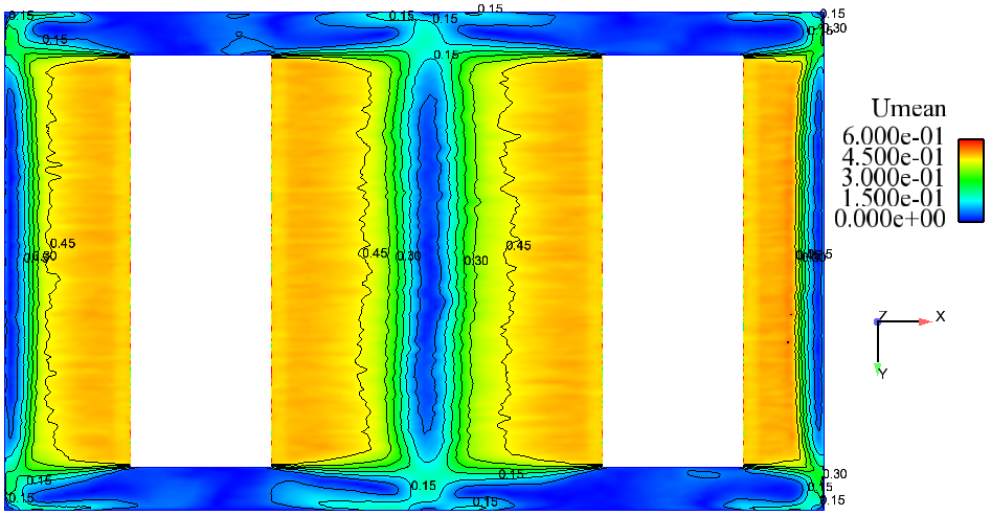

Fig. A-18: Simulation 2. Mean velocity $\overline{u}$ [m/s] on plane $z = 2.95$ m. Averaging time period 120 s.

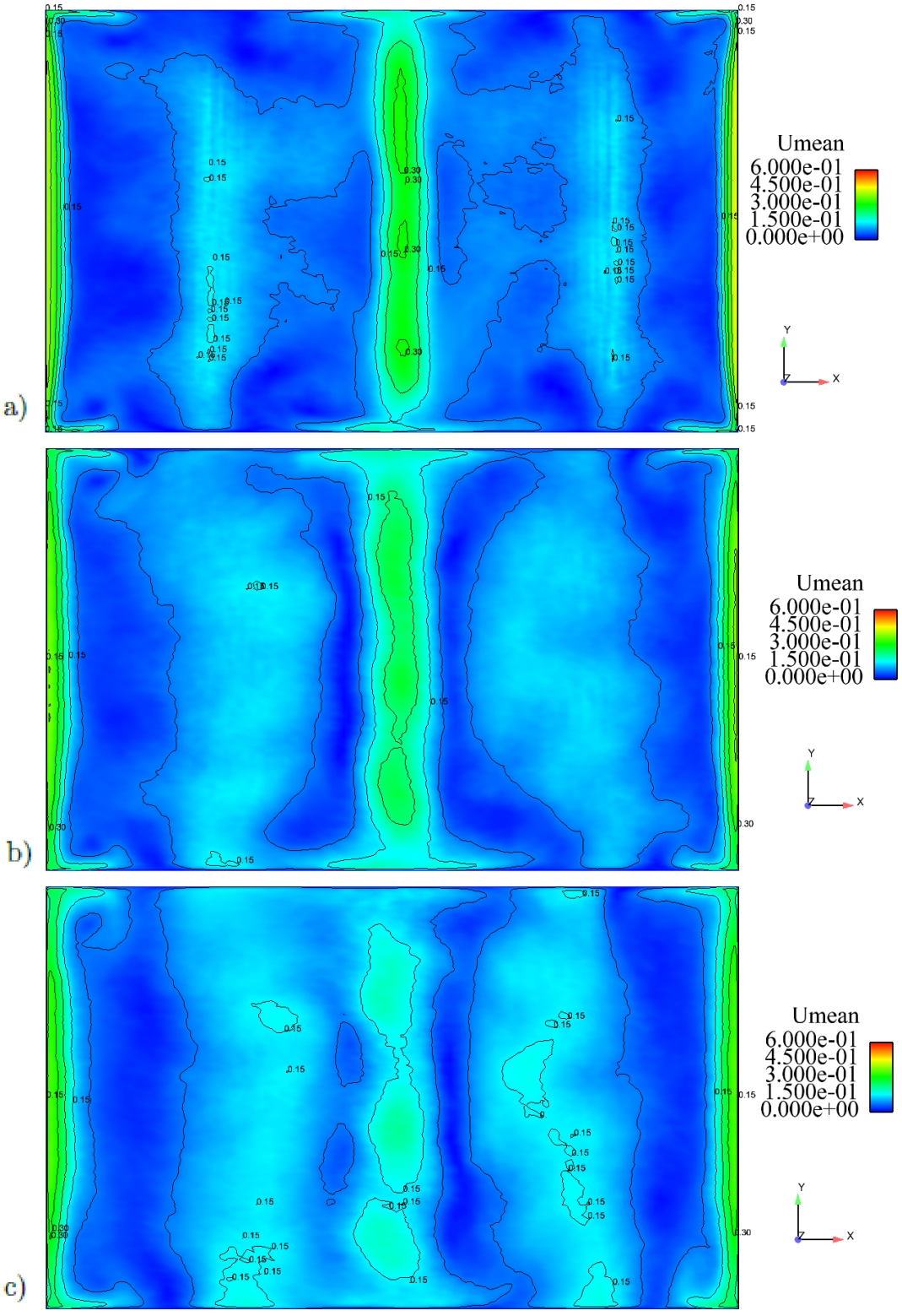

Fig. A-19: Simulation 2. Mean velocity $\overline{u}$ [m/s] on plane a) $z = 2.5$ m b) $z = 2.0$ m c) $z = 1.5$ m. Averaging time period 120 s.

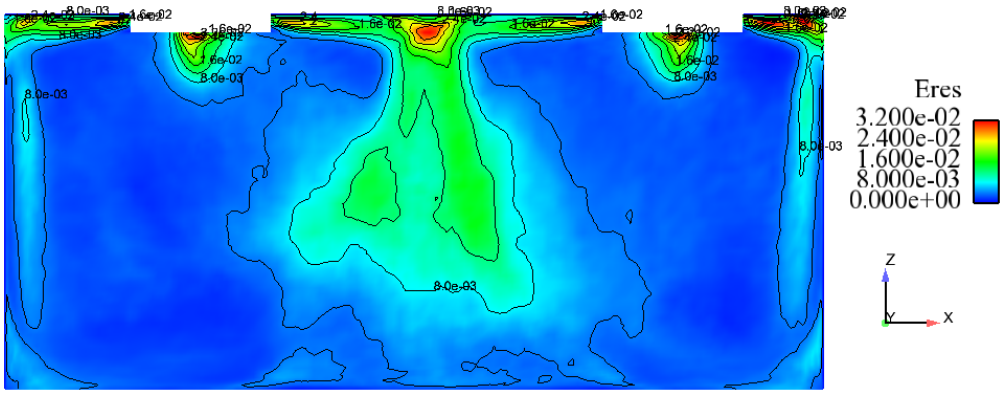

Fig. A-20: Simulation 2. Turbulence kinetic energy $\frac{1}{2}\overline{u'_k u'_k}$ [m^2/s^2] on plane $y = 2$ m. Averaging time period 120 s.

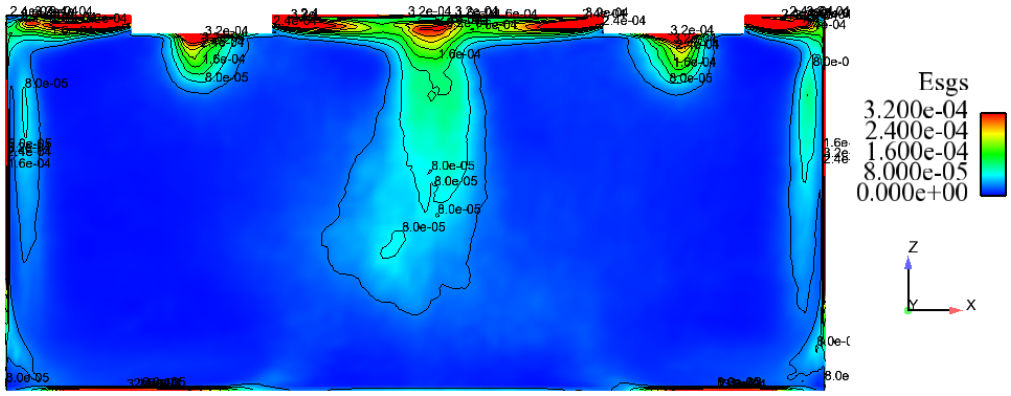

Fig. A-21: Simulation 2. Subgrid-scale turbulence kinetic energy e_{sgs} [m^2/s^2] on plane $y = 2$ m. Averaging time period 120 s.

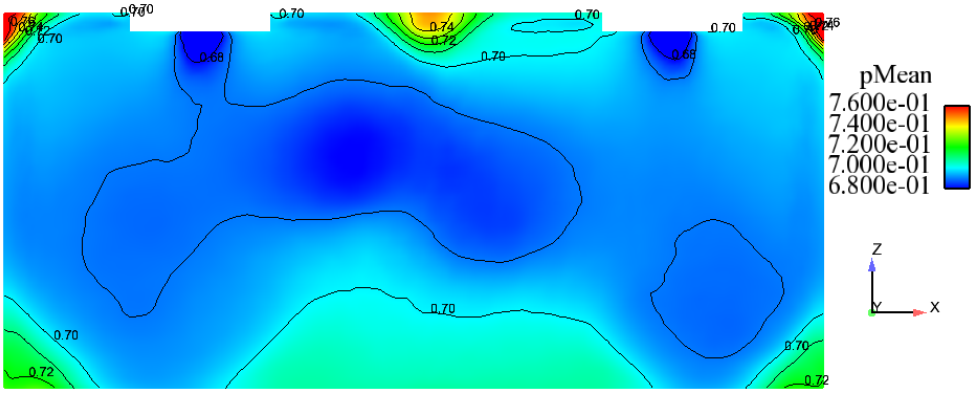

Fig. A-22: Simulation 2. Mean pressure $\overline{p}/\rho$ [m^2/s^2] on plane $y = 2$ m. Averaging time period 120 s.

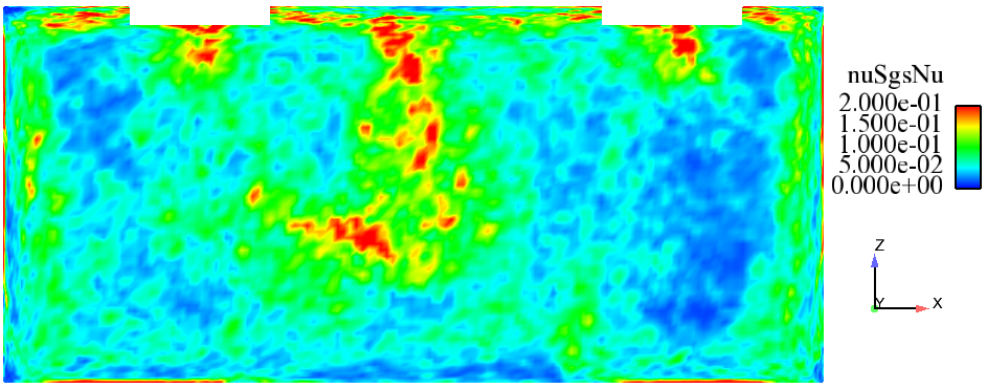

Fig. A-23: Simulation 2. Instantaneous eddy viscosity ν_{sgs}/ν on plane $y = 2$ m.

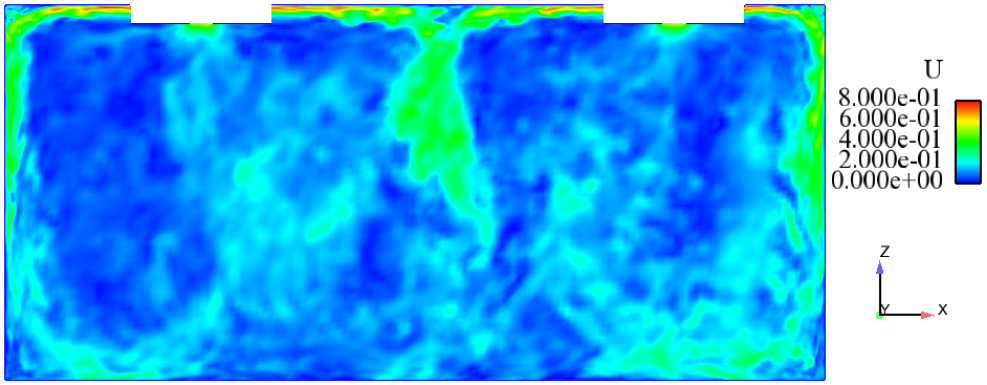

Fig. A-24: Simulation 3. Instantaneous velocity u [m/s] on plane $y = 2$ m.

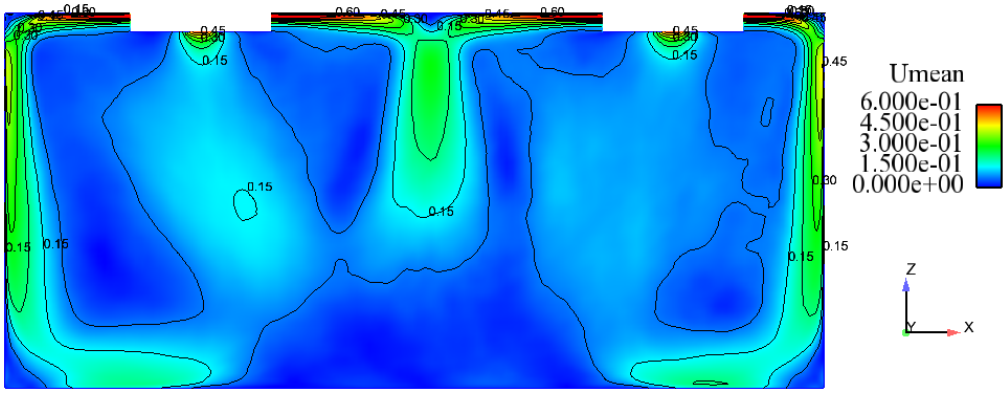

Fig. A-25: Simulation 3. Mean velocity $\overline{u}$ [m/s] on plane $y = 2$ m. Averaging time period 120 s.

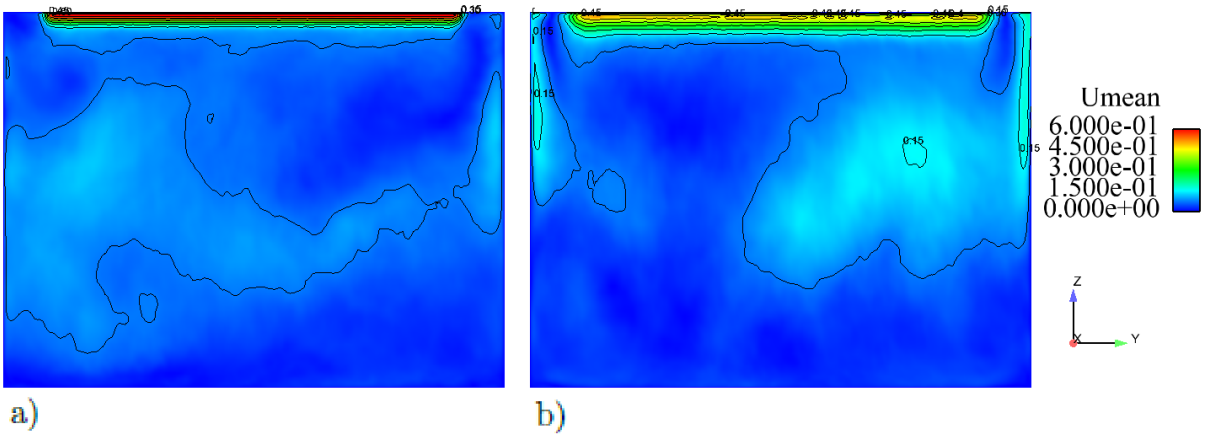

Fig. A-26: Simulation 3. Mean velocity $\overline{u}$ [m/s] on plane a) $x = 2.5$ m b) $x = 3.0$ m. Averaging time period 120 s.

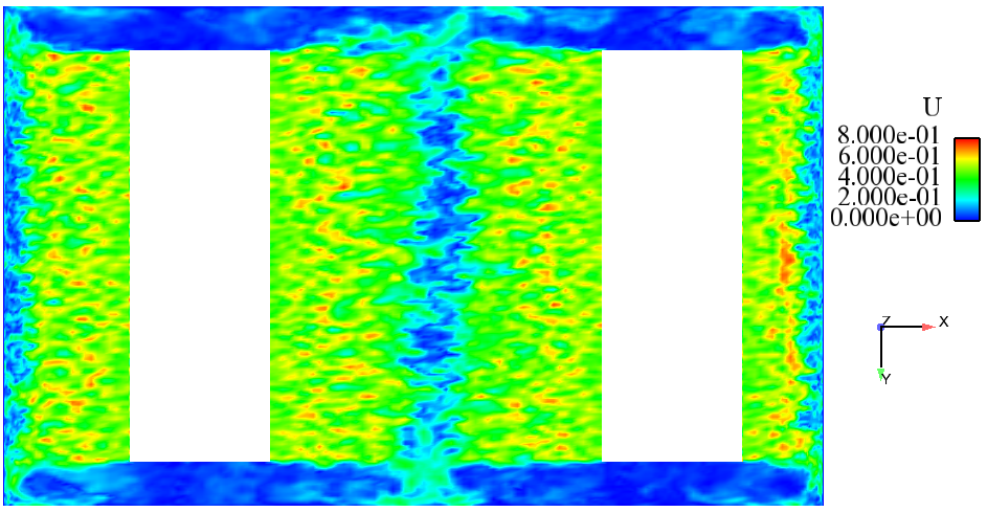

Fig. A-27: Simulation 3. Instantaneous velocity u [m/s] on plane $z = 2.95$ m.

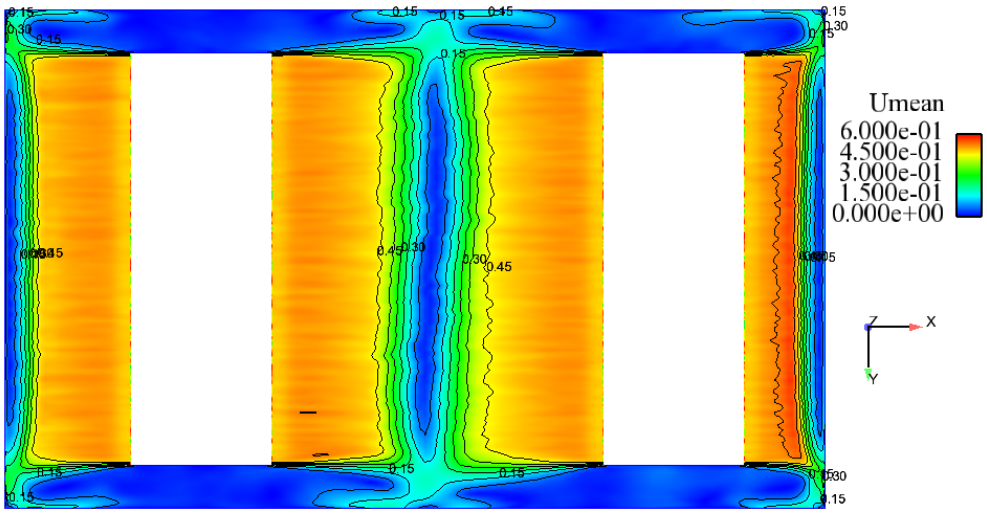

Fig. A-28: Simulation 3. Mean velocity $\overline{u}$ [m/s] on plane $z = 2.95$ m. Averaging time period 120 s.

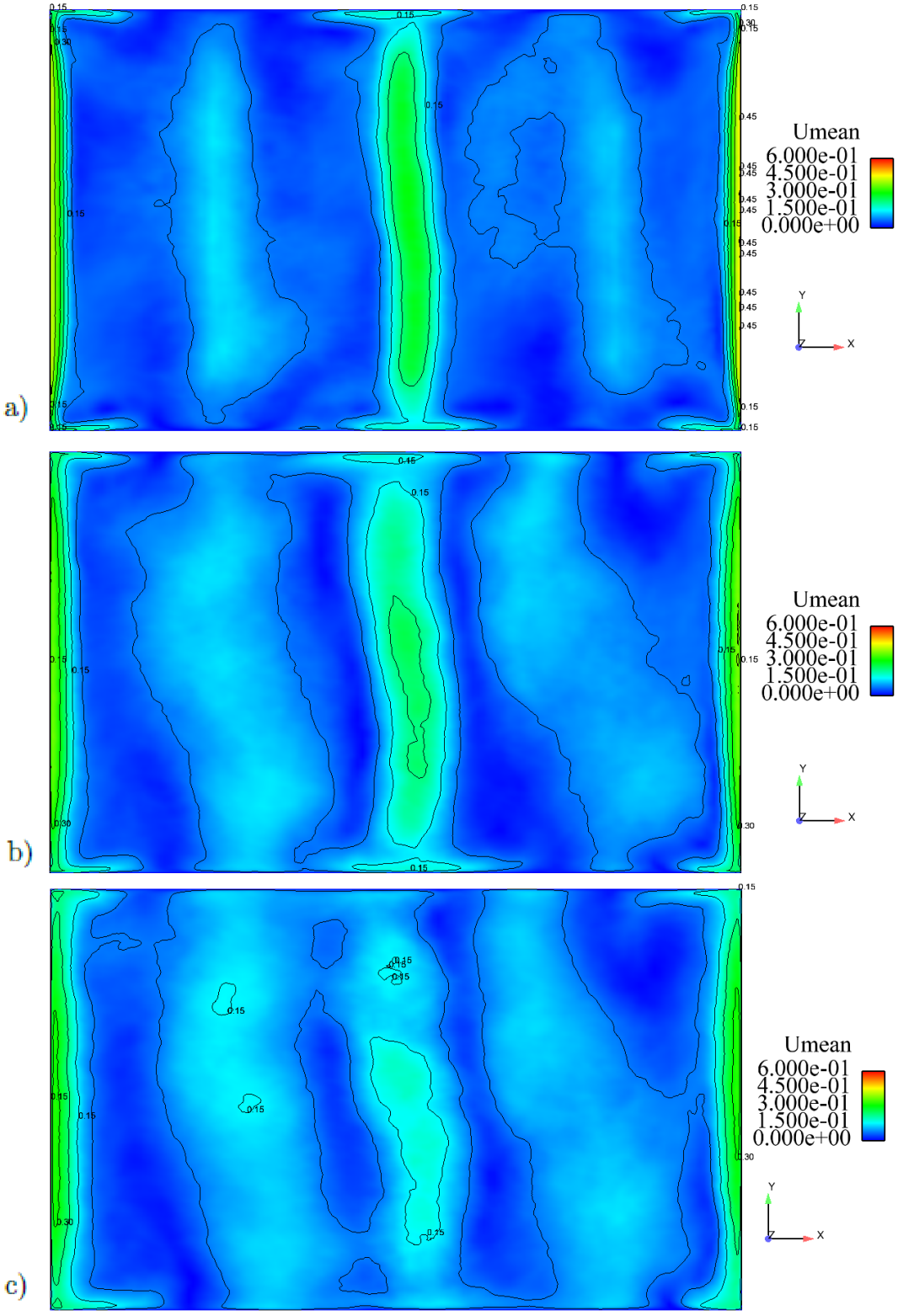

Fig. A-29: Simulation 3. Mean velocity $\overline{u}$ [m/s] on plane a) $z = 2.5$ m b) $z = 2.0$ m c) $z = 1.5$ m. Averaging time period 120 s.

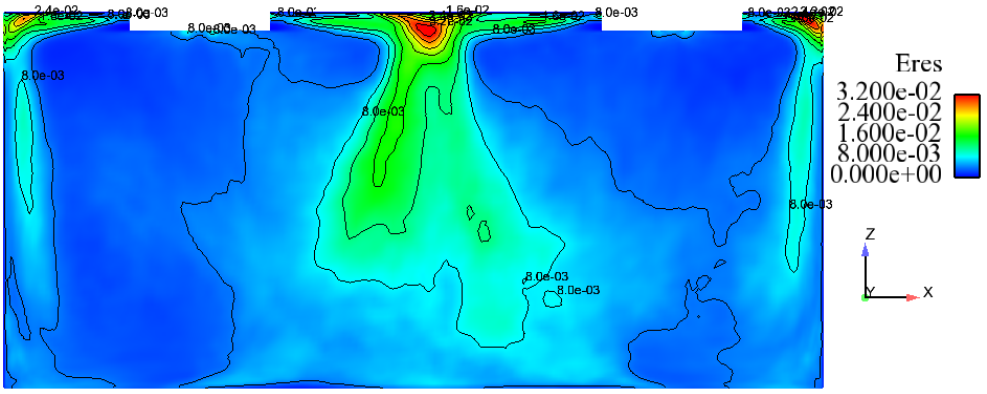

Fig. A-30: Simulation 3. Turbulence kinetic energy $\frac{1}{2}\overline{u'_k u'_k}$ [m^2/s^2] on plane $y = 2$ m. Averaging time period 120 s.

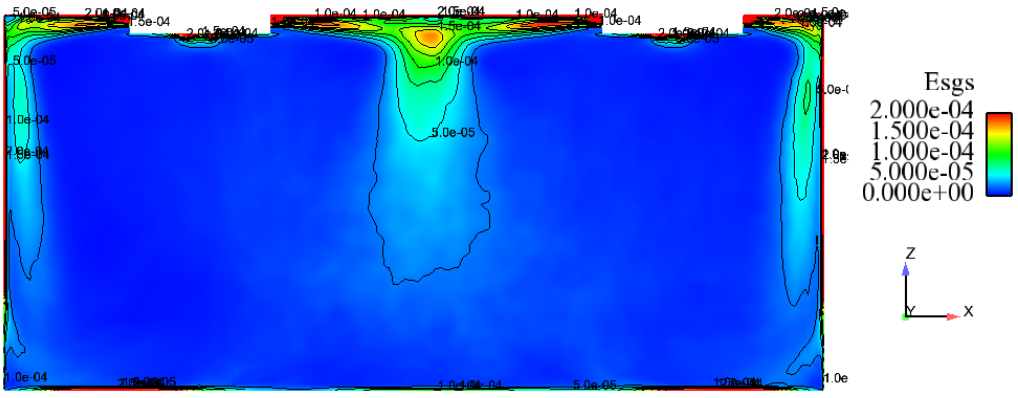

Fig. A-31: Simulation 3. Subgrid-scale turbulence kinetic energy e_{sgs} [m^2/s^2] on plane $y = 2$ m . Averaging time period 120 s.

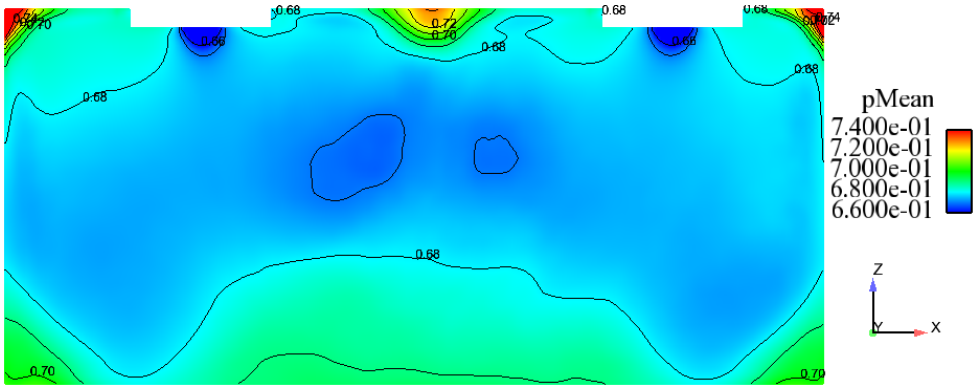

Fig. A-32: Simulation 3. Mean pressure $\overline{p}/\rho$ [m^2/s^2] on plane $y = 2$ m. Averaging time period 120 s.

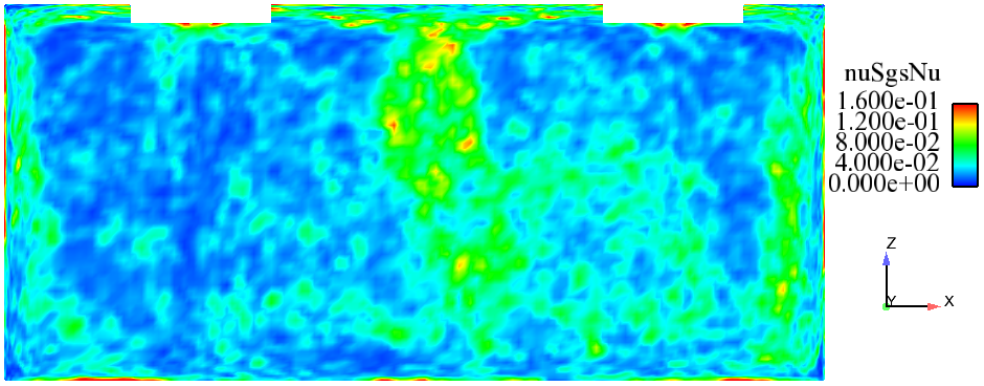

Fig. A-33: Simulation 3. Instantaneous eddy viscosity ν_{sgs}/ν on plane $y = 2$ m.

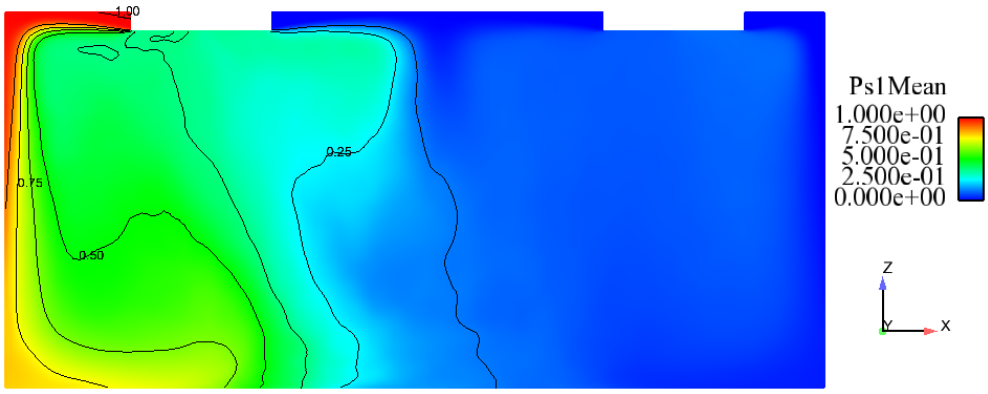

Fig. A-34: Simulation 3. Mean passive scalar $\overline{\theta}_1$ on plane $y = 2$ m. Averaging time period 120 s.

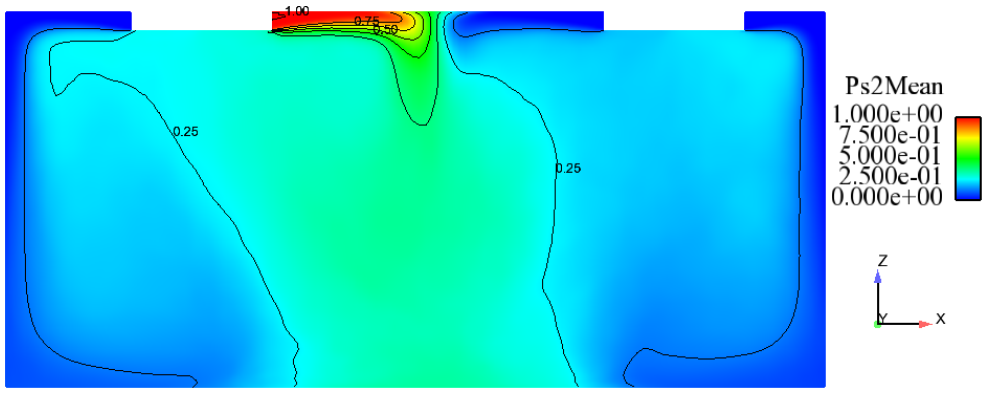

Fig. A-35: Simulation 3. Mean passive scalar $\overline{\theta}_2$ on plane $y = 2$ m. Averaging time period 120 s.

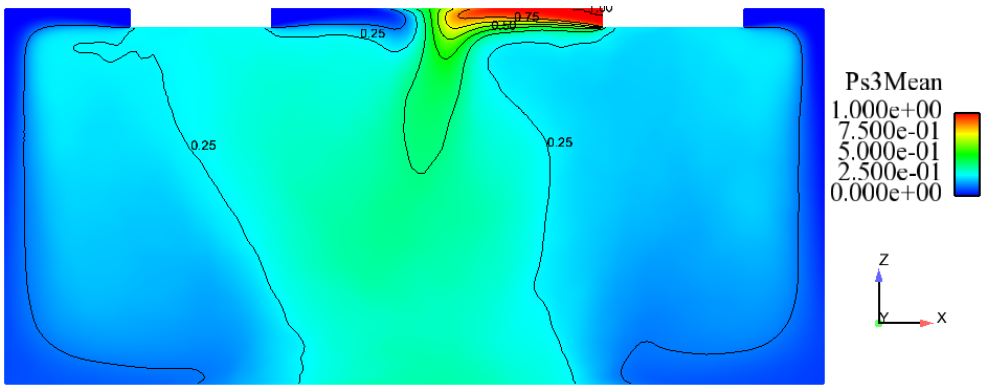

Fig. A-36: Simulation 3. Mean passive scalar $\overline{\theta}_3$ on plane $y = 2$ m. Averaging time period 120 s.

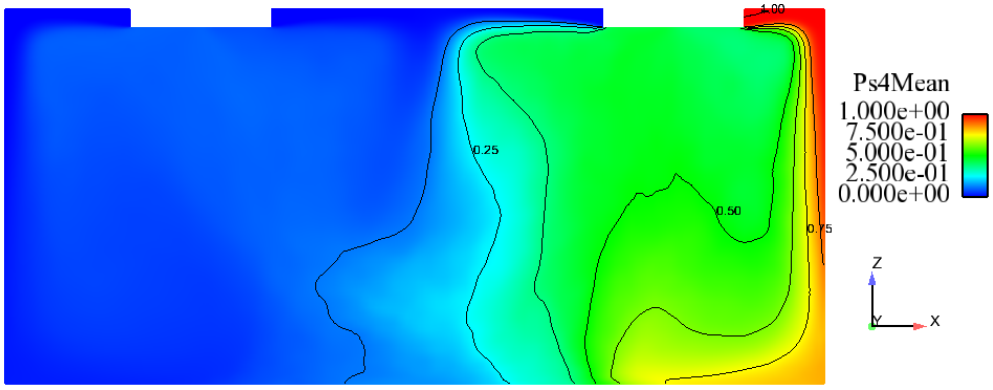

Fig. A-37: Simulation 3. Mean passive scalar $\overline{\theta}_4$ on plane $y = 2$ m. Averaging time period 120 s.

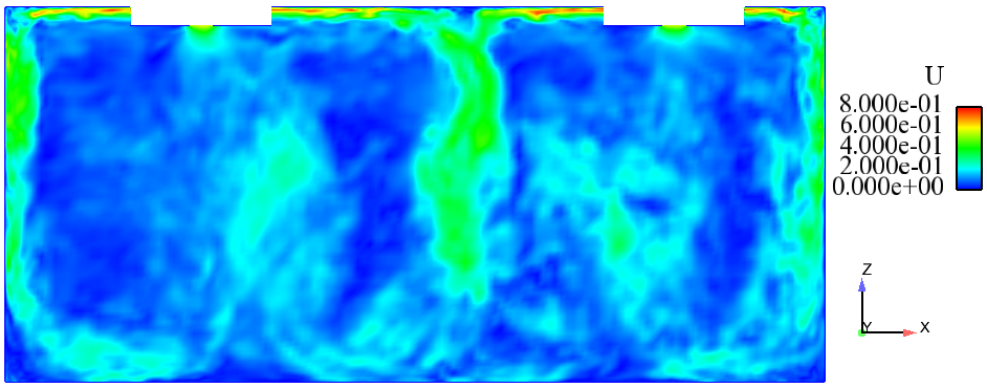

Fig. A-38: Simulation 4. Instantaneous velocity u [m/s] on plane $y = 2$ m

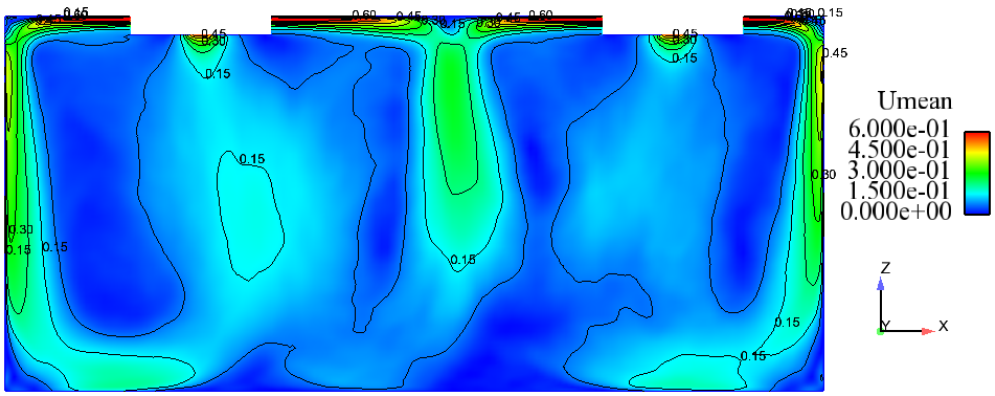

Fig. A-39: Simulation 4. Mean velocity $\overline{u}$ [m/s] on plane $y = 2$ m. Averaging time period 150 s.

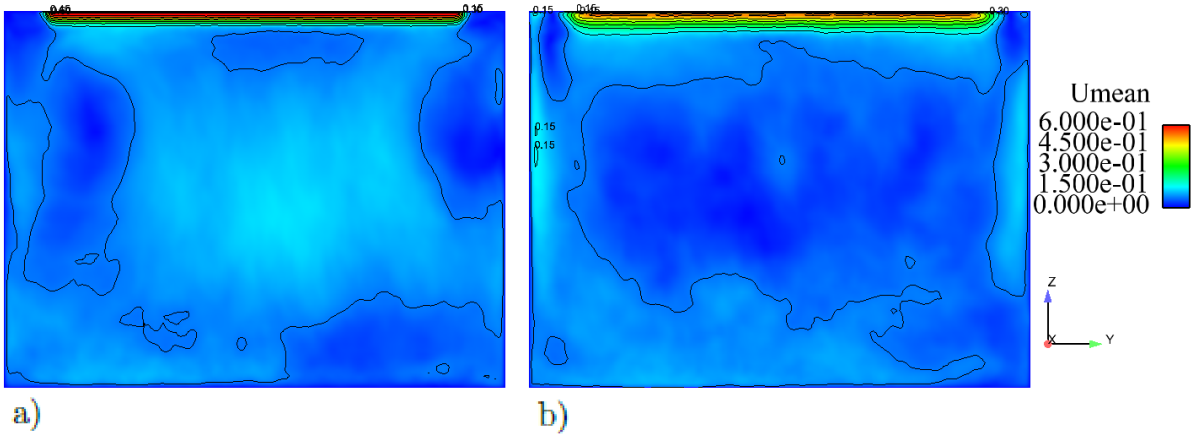

Fig. A-40: Simulation 4. Mean velocity $\overline{u}$ [m/s] on plane a) $x = 2.5$ m b) $x = 3.0$ m. Averaging time period 120 s.

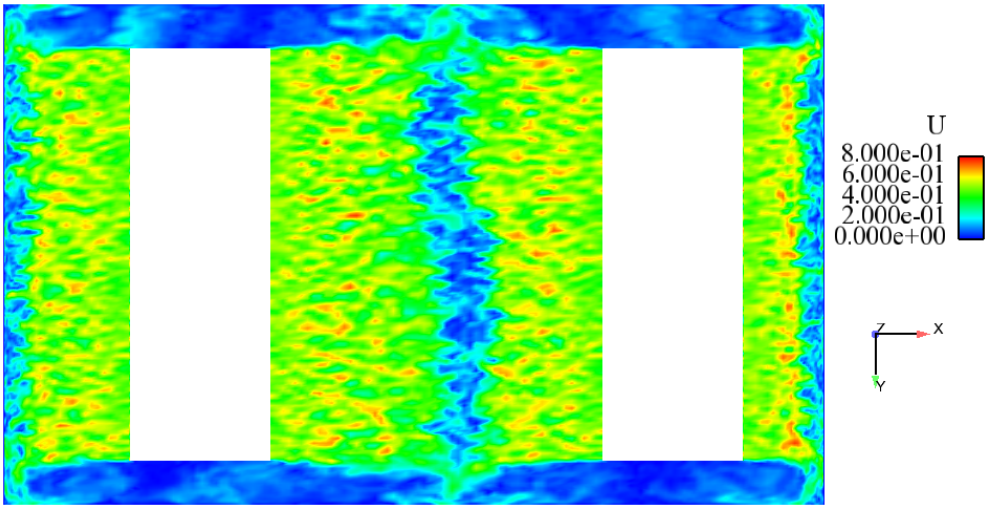

Fig. A-41: Simulation 4. Instantaneous velocity u [m/s] on plane $z = 2.95$ m.

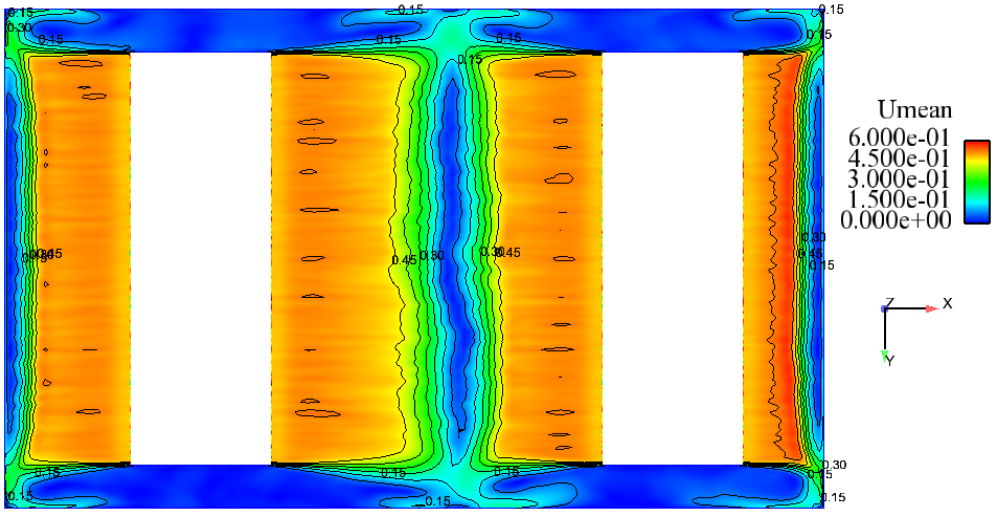

Fig. A-42: Simulation 4. Mean velocity $\overline{u}$ [m/s] on plane $z = 2.95$ m. Averaging time period 150 s.

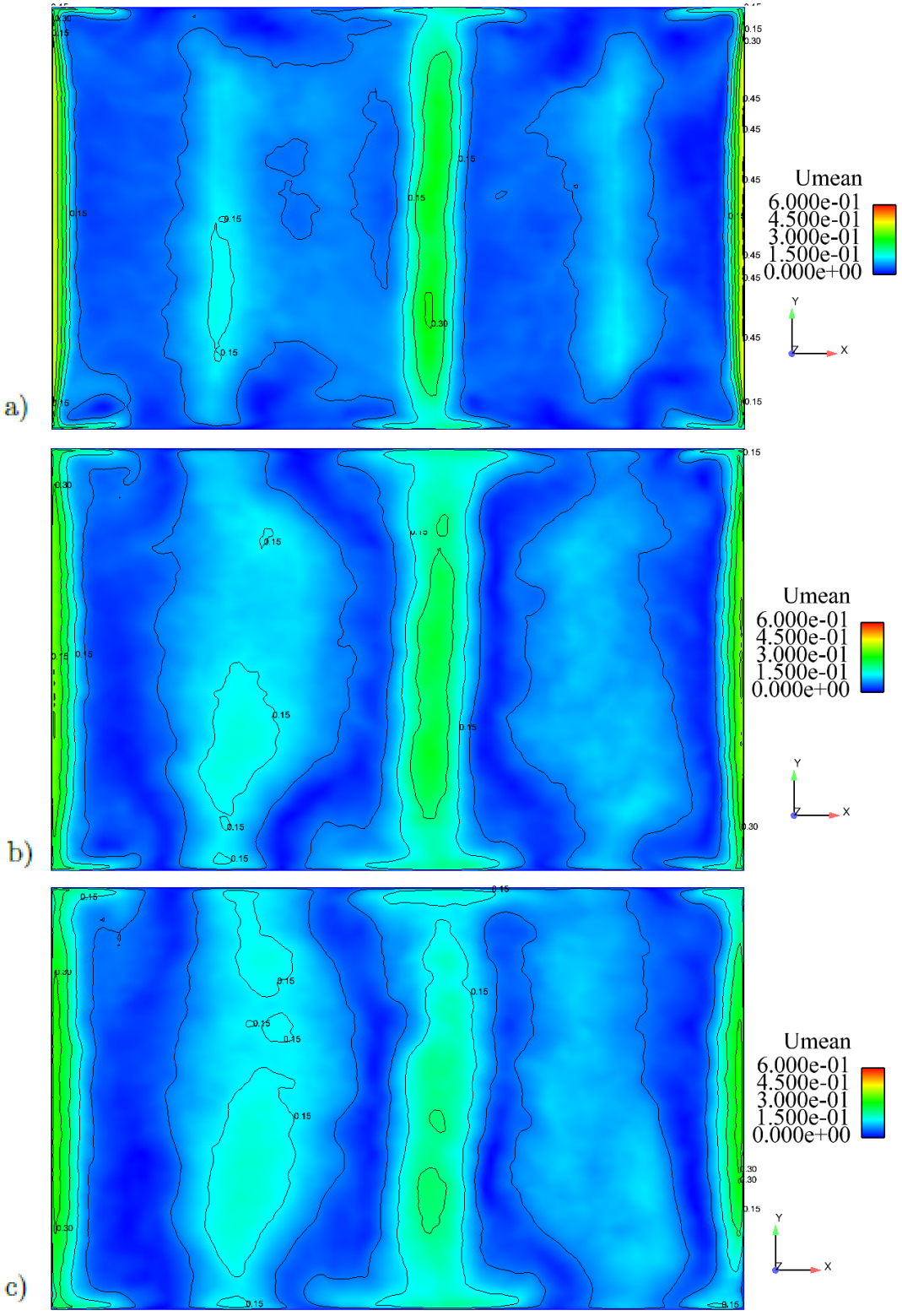

Fig. A-43: Simulation 4. Mean velocity $\overline{u}$ [m/s] on plane a) $z = 2.5$ m b) $z = 2.0$ m c) $z = 1.5$ m. Averaging time period 120 s.

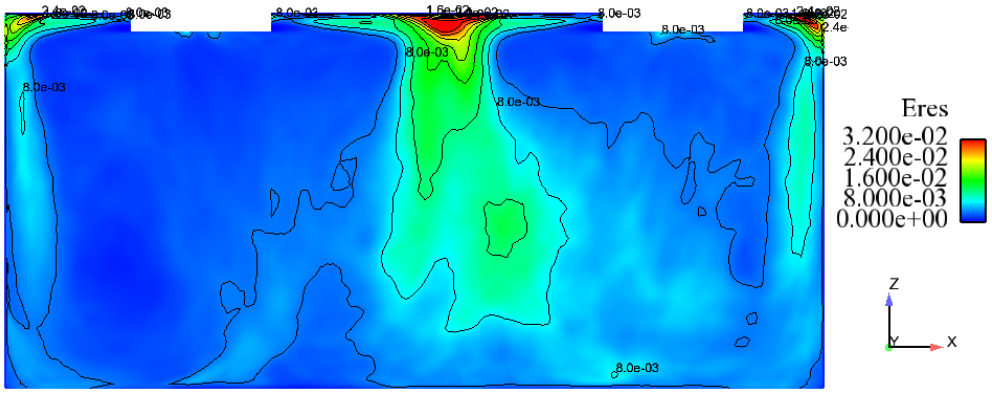

Fig. A-44: Simulation 4. Turbulence kinetic energy $\frac{1}{2}\overline{u'_k u'_k}$ [m^2/s^2] on plane $y = 2$ m. Averaging time period 150 s.

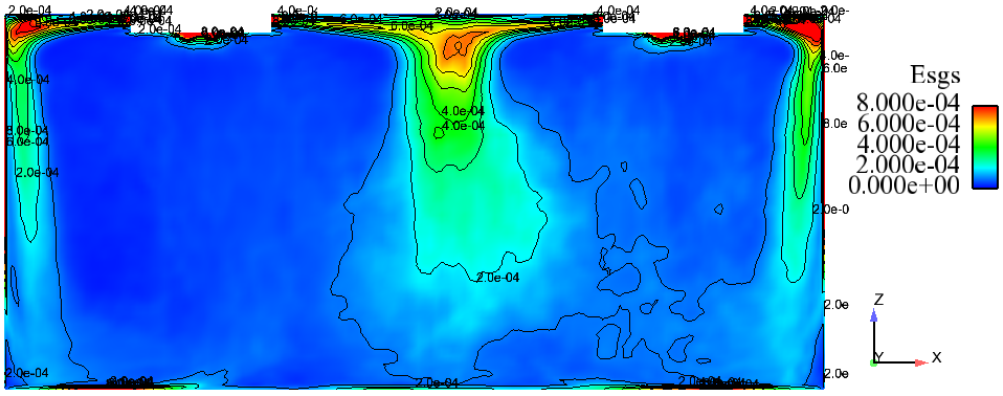

Fig. A-45: Simulation 4. Subgrid-scale turbulence kinetic energy e_{sgs} [m^2/s^2] on plane $y = 2$ m . Averaging time period 150 s.

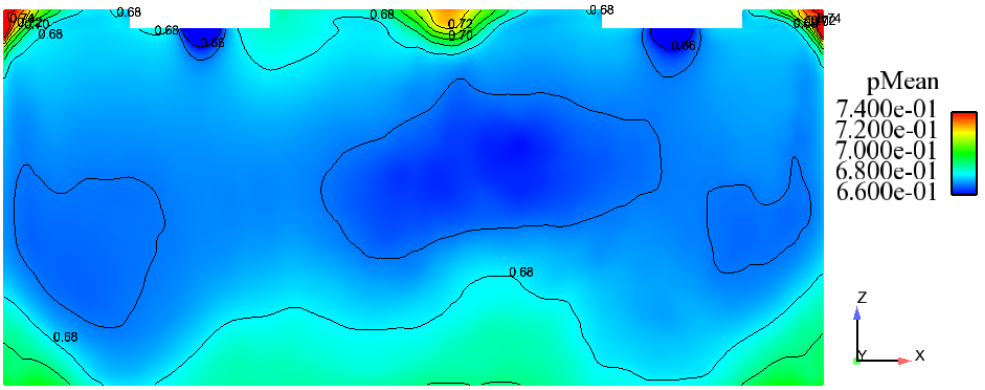

Fig. A-46: Simulation 4. Mean pressure $\overline{p}/\rho$ [m^2/s^2] on plane $y = 2$ m. Averaging time period 150 s.

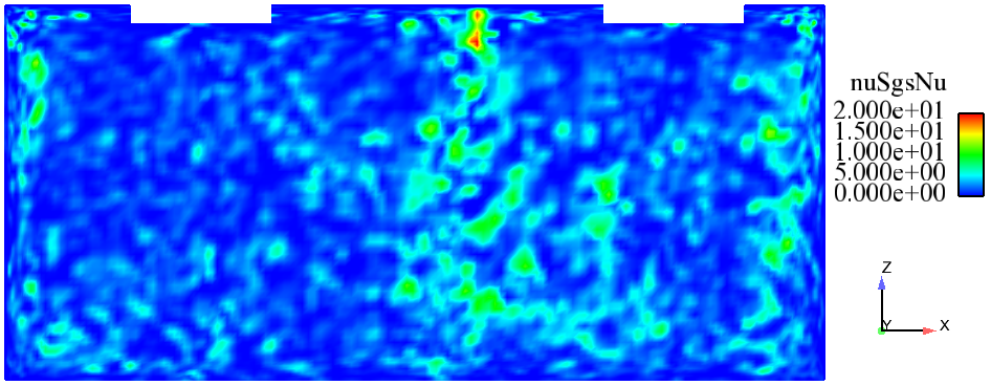

Fig. A-47: Simulation 4. Instantaneous eddy viscosity ν_{sgs}/ν on plane $y = 2$ m.

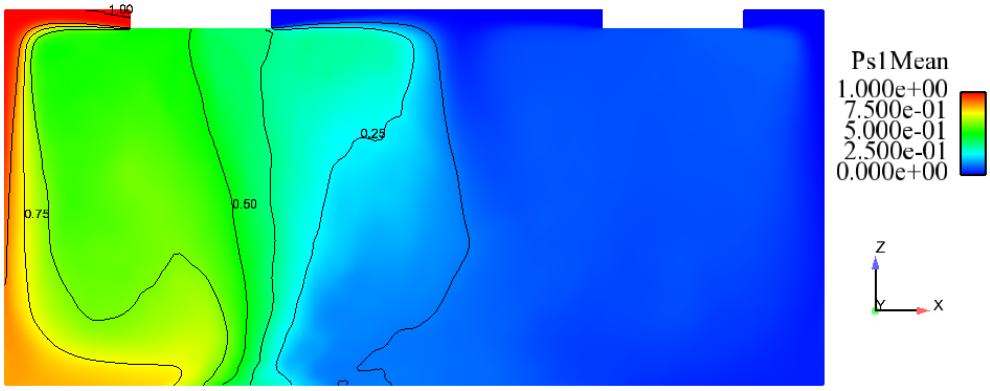

Fig. A-48: Simulation 4. Mean passive scalar $\overline{\theta}_1$ on plane $y = 2$ m. Averaging time period 150 s.

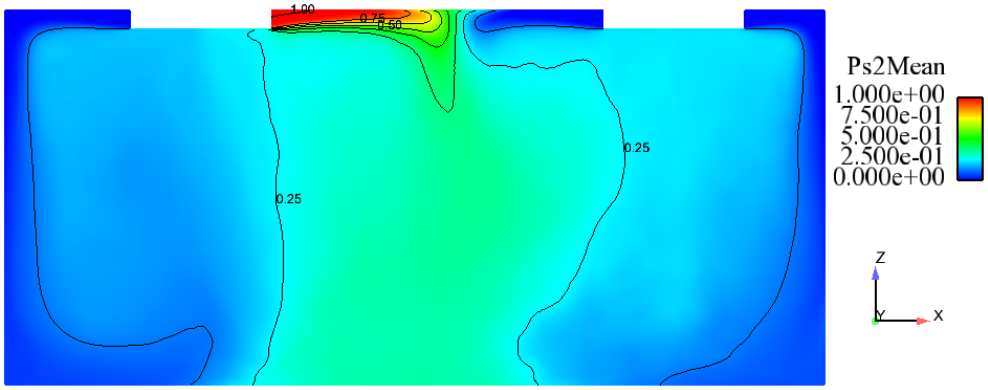

Fig. A-49: Simulation 4. Mean passive scalar $\overline{\theta}_2$ on plane $y = 2$ m. Averaging time period 150 s.

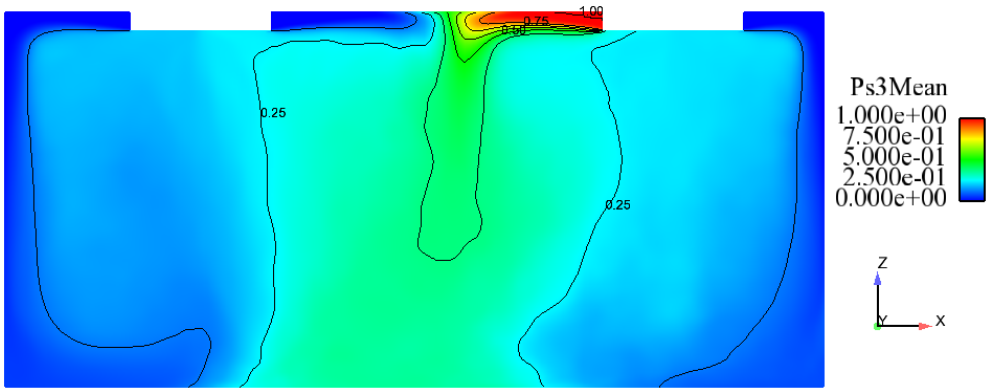

Fig. A-50: Simulation 4. Mean passive scalar $\overline{\theta}_3$ on plane $y = 2$ m. Averaging time period 150 s.

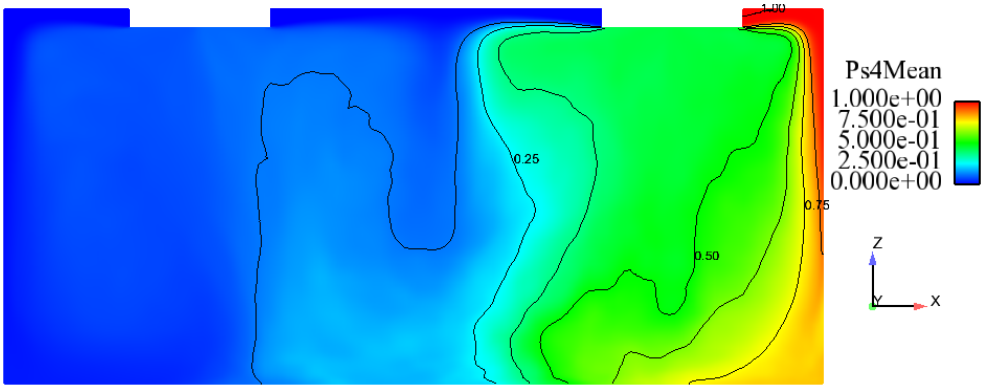

Fig. A-51: Simulation 4. Mean passive scalar $\overline{\theta}_4$ on plane $y = 2$ m. Averaging time period 150 s.

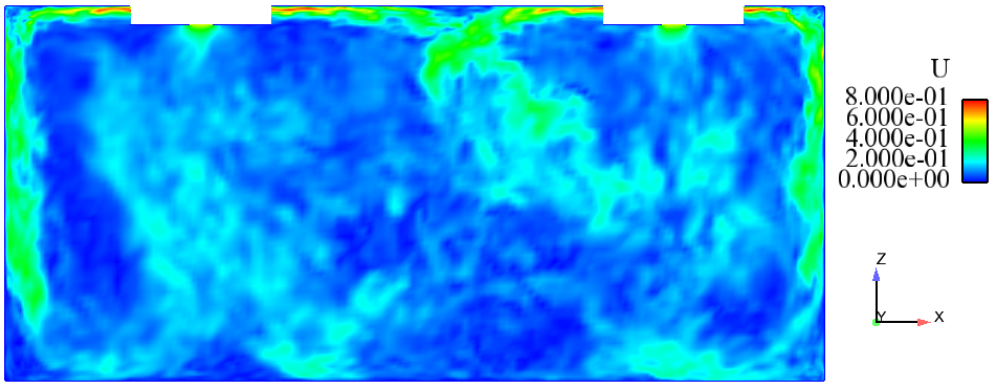

Fig. A-52: Simulation 5. Instantaneous velocity u [m/s] on plane $y = 2$ m.

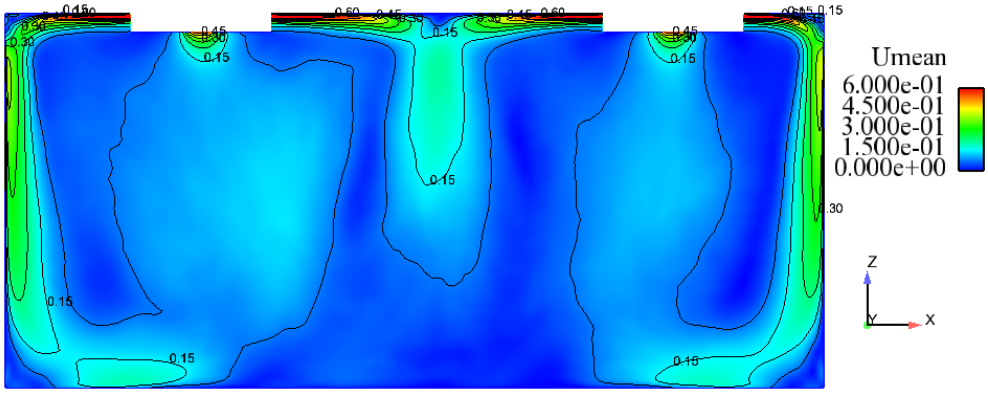

Fig. A-53: Simulation 5. Mean velocity $\overline{u}$ [m/s] on plane $y = 2$ m. Averaging time period 120 s.

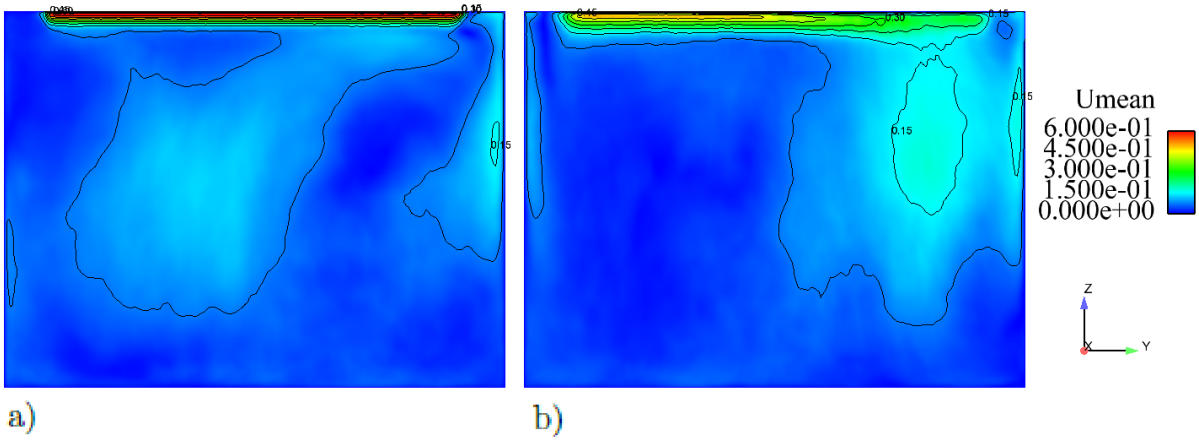

Fig. A-54: Simulation 5. Mean velocity $\overline{u}$ [m/s] on plane a) $x = 2.5$ m b) $x = 3.0$ m. Averaging time period 120 s.

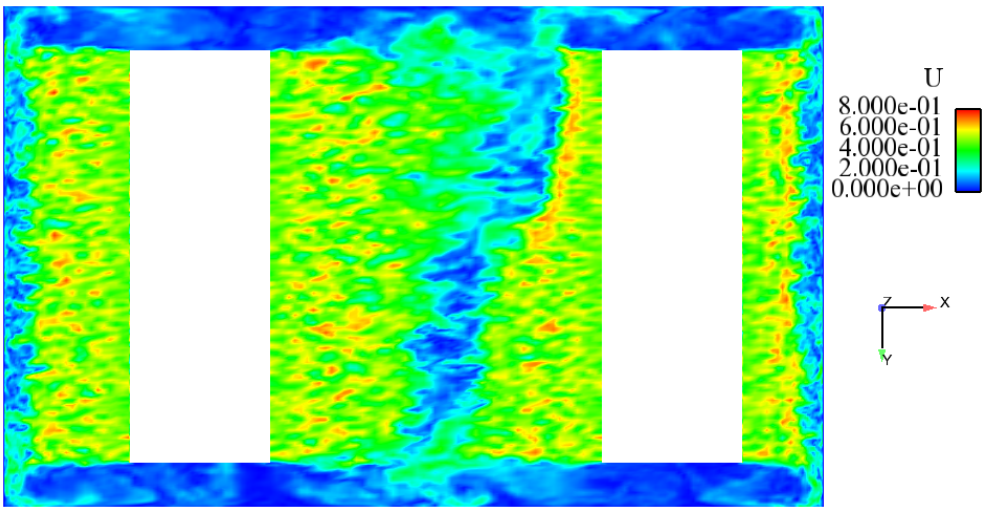

Fig. A-55: Simulation 5. Instantaneous velocity u [m/s] on plane $z = 2.95$ m.

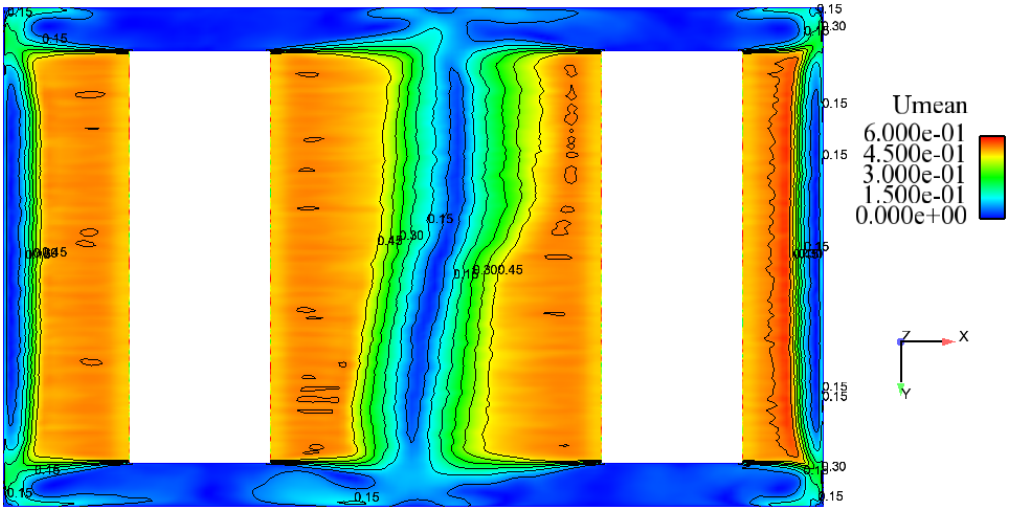

Fig. A-56: Simulation 5. Mean velocity $\overline{u}$ [m/s] on plane $z = 2.95$ m. Averaging time period 120 s.

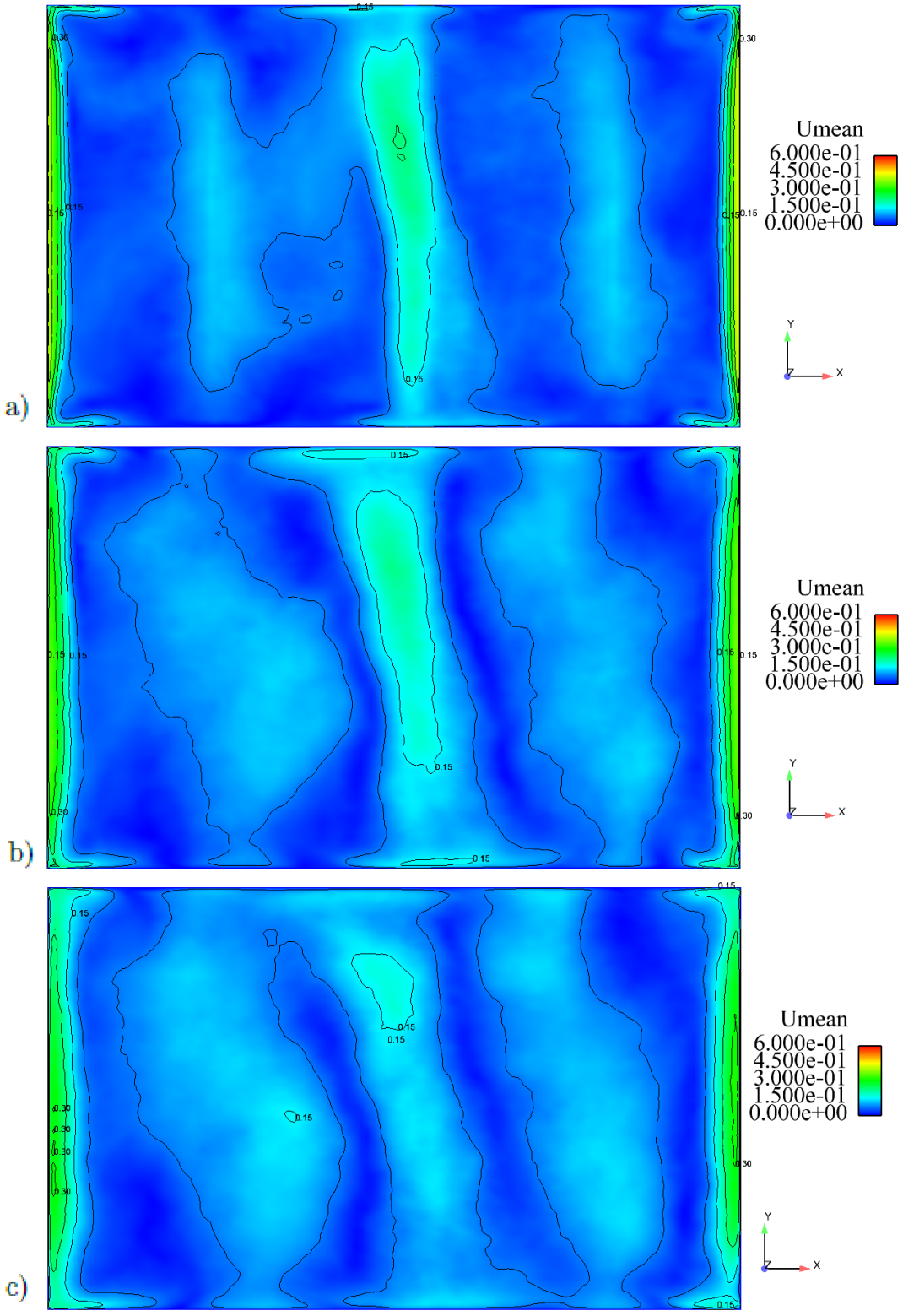

Fig. A-57: Simulation 5. Mean velocity $\overline{u}$ [m/s] on plane a) $z = 2.5$ m b) $z = 2.0$ m c) $z = 1.5$ m. Averaging time period 120 s.

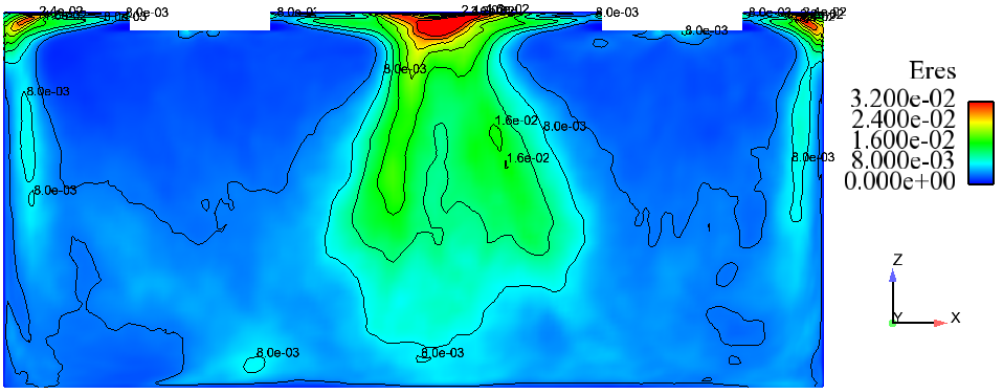

Fig. A-58: Simulation 5. Turbulence kinetic energy $\frac{1}{2}\overline{u'_k u'_k}$ [m^2/s^2] on plane $y = 2$ m. Averaging time period 120 s.

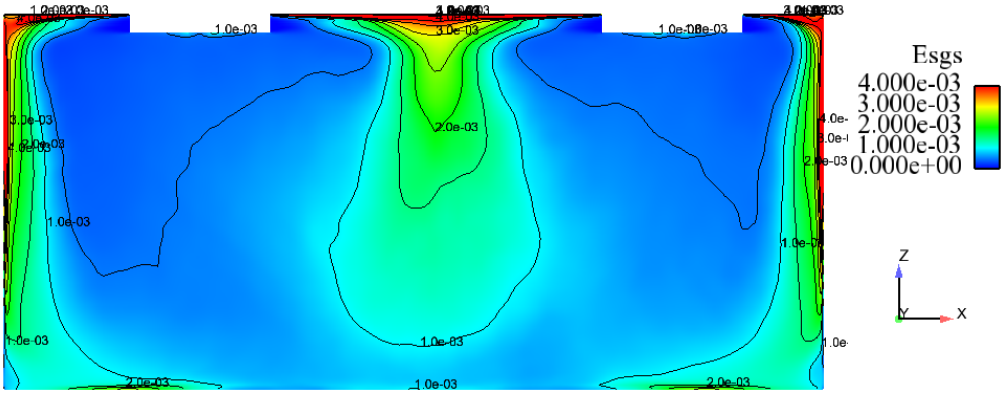

Fig. A-59: Simulation 5. Subgrid-scale turbulence kinetic energy e_{sgs} [m^2/s^2] on plane $y = 2$ m. Averaging time period 120 s.

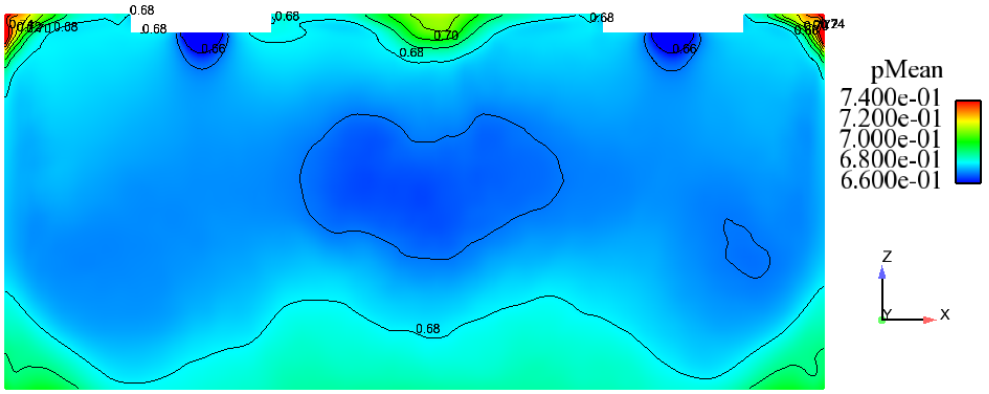

Fig. A-60: Simulation 5. Mean pressure $\overline{p}/\rho$ [m^2/s^2] on plane $y = 2$ m. Averaging time period 120 s.

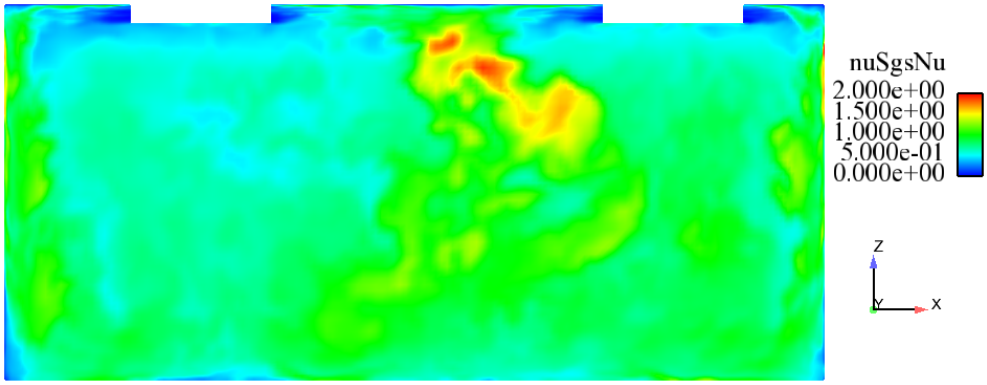

Fig. A-61: Simulation 5. Instantaneous eddy viscosity ν_{sgs}/ν on plane $y = 2$ m.

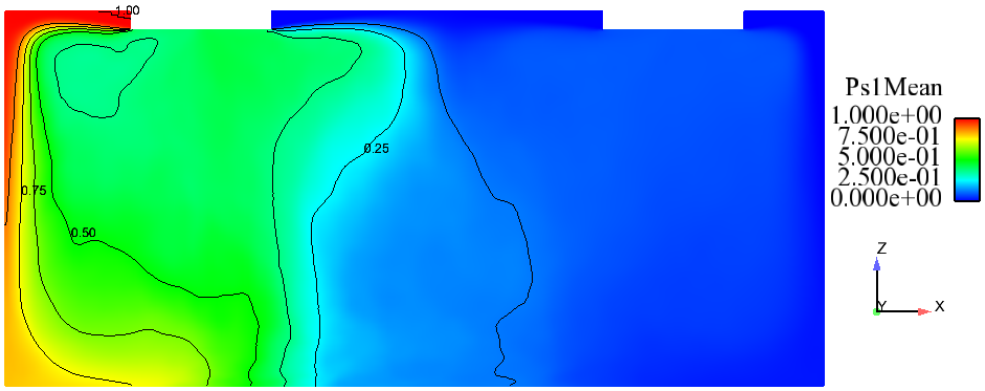

Fig. A-62: Simulation 5. Mean passive scalar $\overline{\theta}_1$ on plane $y = 2$ m. Averaging time period 120 s.

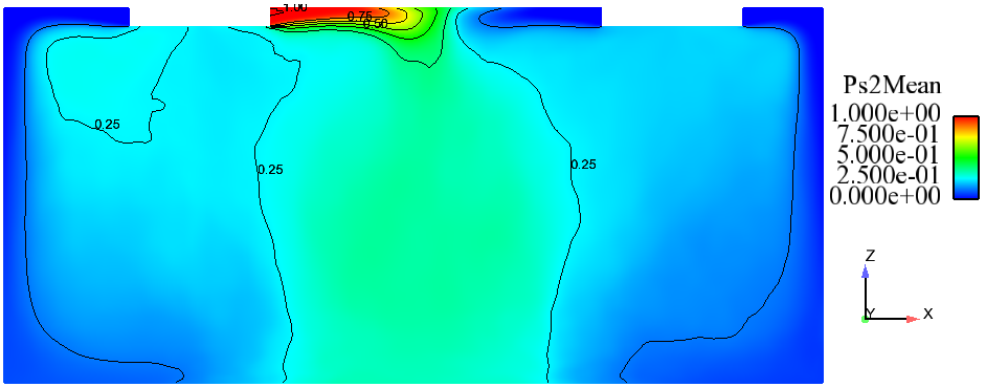

Fig. A-63: Simulation 5. Mean passive scalar $\overline{\theta}_2$ on plane $y = 2$ m. Averaging time period 120 s.

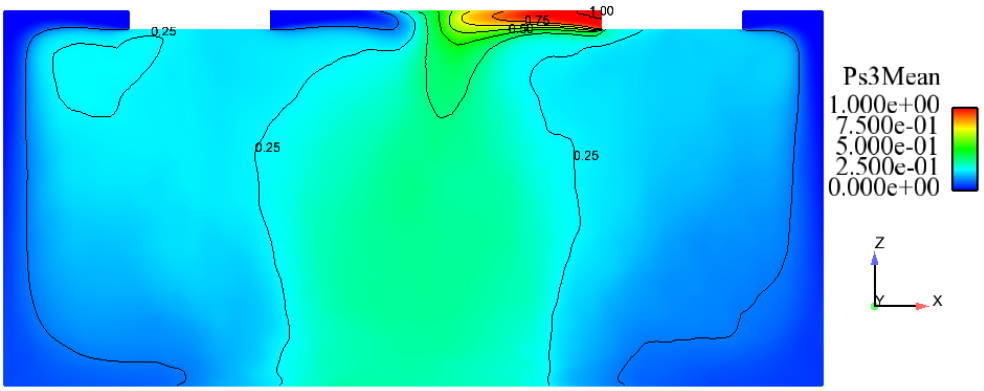

Fig. A-64: Simulation 5. Mean passive scalar $\overline{\theta}_3$ on plane $y = 2$ m. Averaging time period 120 s.

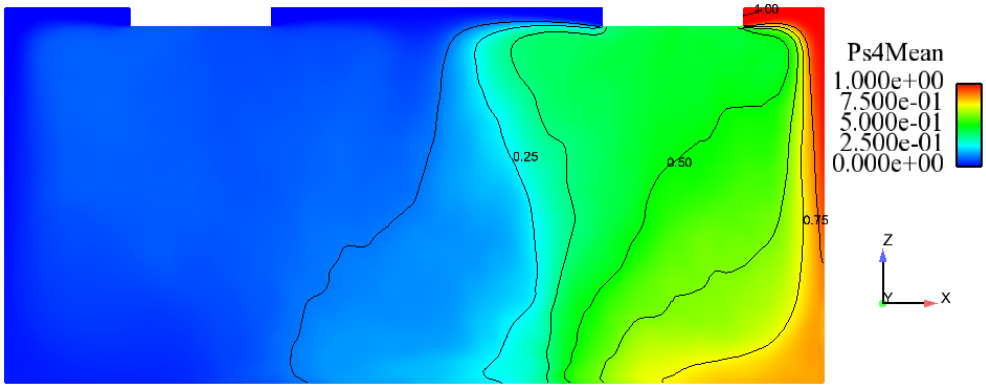

Fig. A-65: Simulation 5. Mean passive scalar $\overline{\theta}_4$ on plane $y = 2$ m. Averaging time period 120 s.

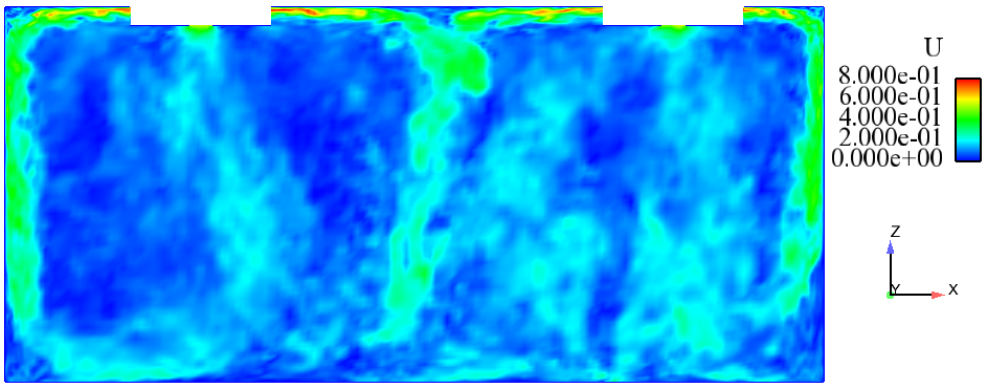

Fig. A-66: Simulation 6. Instantaneous velocity u [m/s] on plane $y = 2$ m.

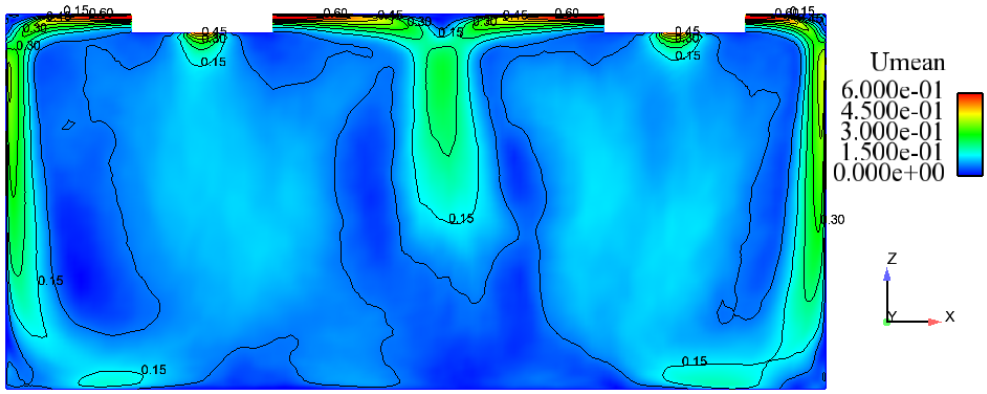

Fig. A-67: Simulation 6. Mean velocity $\overline{u}$ [m/s] on plane $y = 2$ m. Averaging time period 120 s.

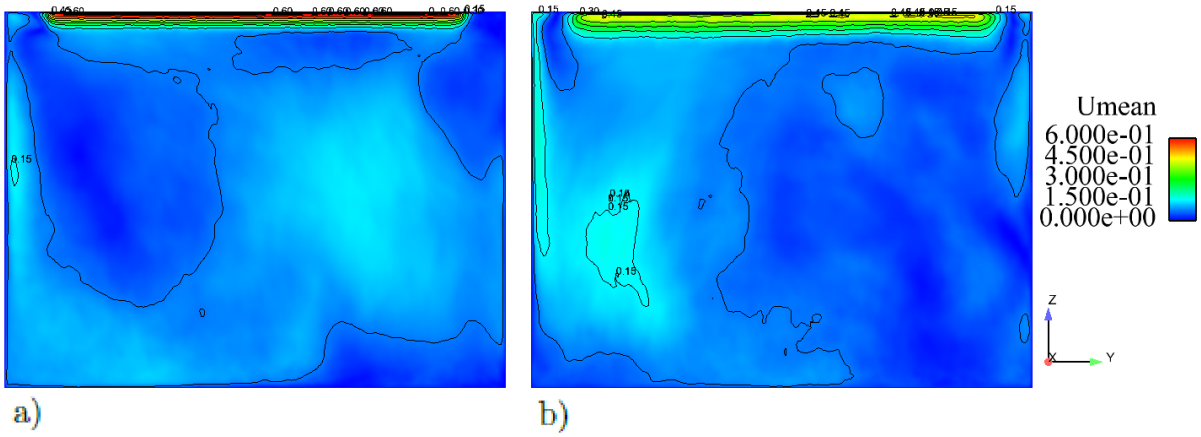

Fig. A-68: Simulation 6. Mean velocity $\overline{u}$ [m/s] on plane a) $x = 2.5$ m b) $x = 3.0$ m. Averaging time period 120 s.

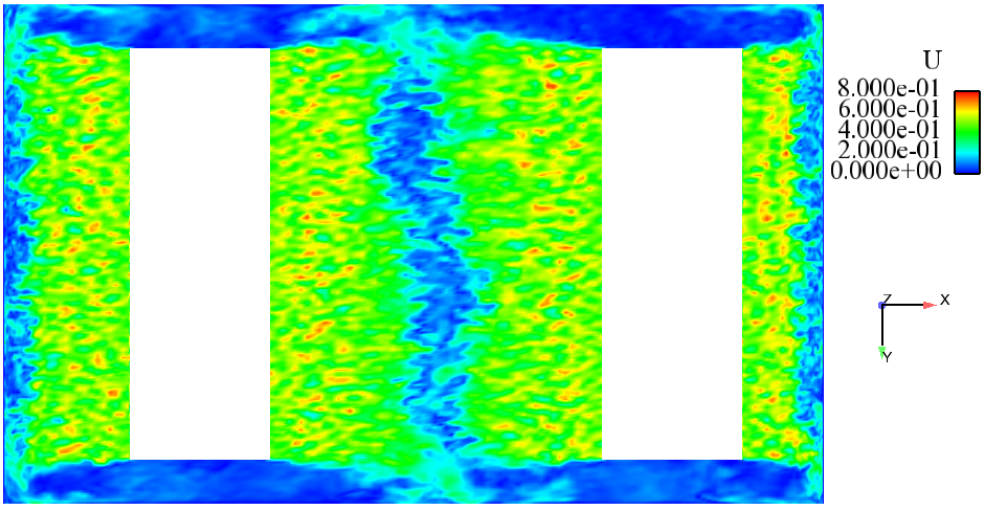

Fig. A-69: Simulation 6. Instantaneous velocity u [m/s] on plane $z = 2.95$ m.

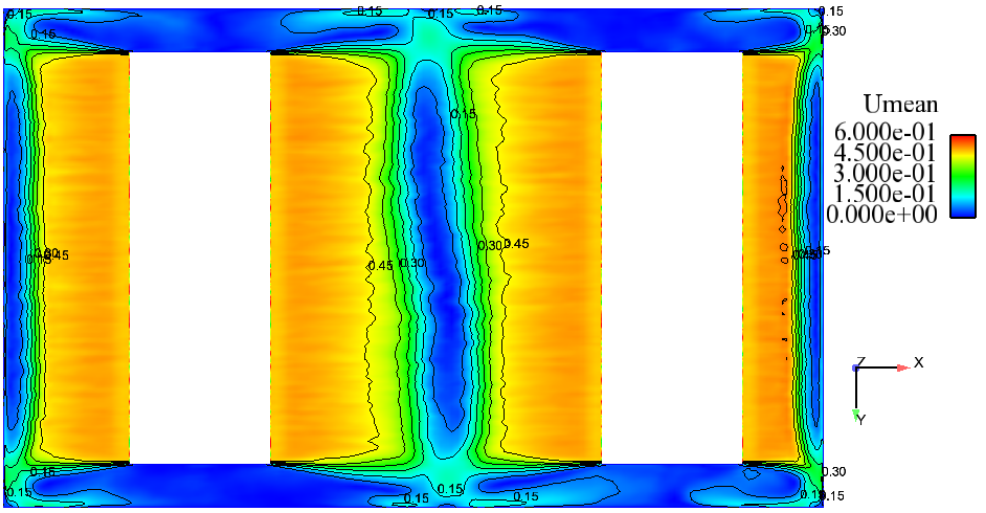

Fig. A-70: Simulation 6. Mean velocity $\overline{u}$ [m/s] on plane $z = 2.95$ m. Averaging time period 120 s.

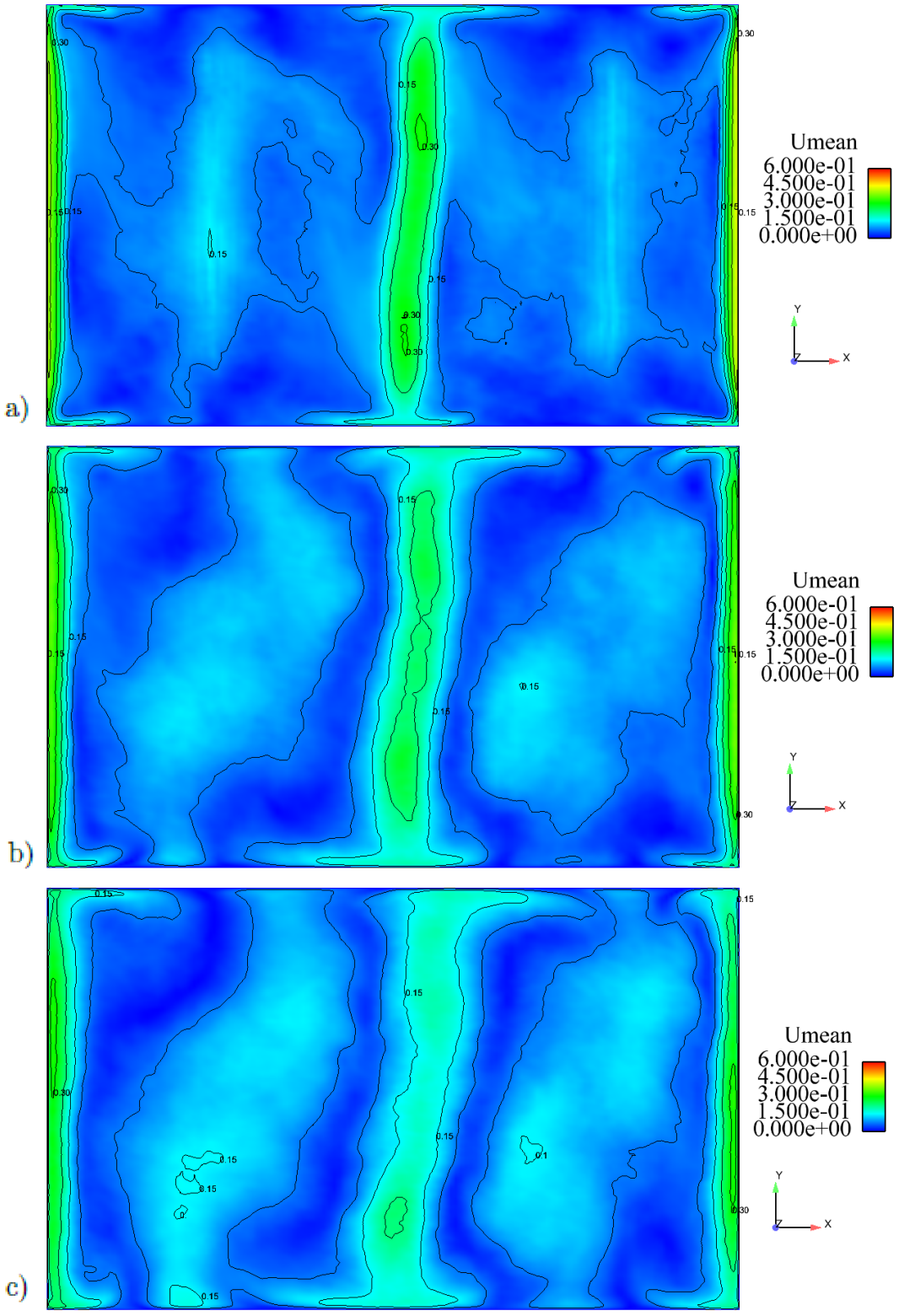

Fig. A-71: Simulation 6. Mean velocity $\overline{u}$ [m/s] on plane a) $z = 2.5$ m b) $z = 2.0$ m c) $z = 1.5$ m. Averaging time period 120 s.

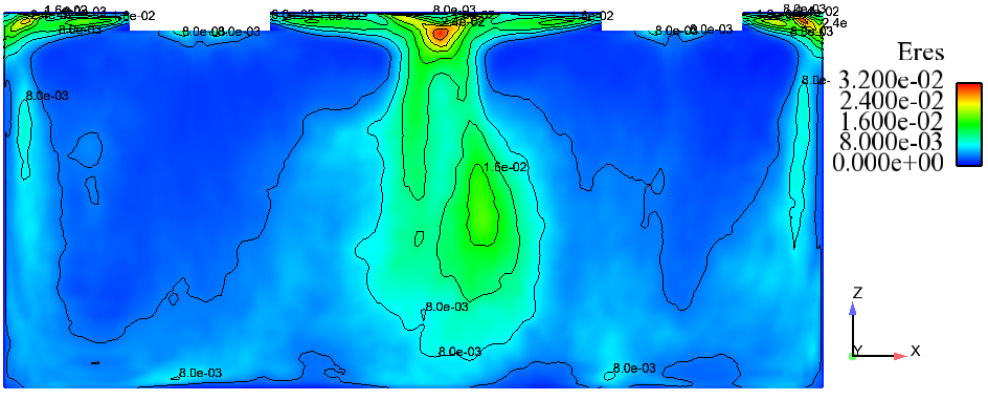

Fig. A-72: Simulation 6. Turbulence kinetic energy $\frac{1}{2}\overline{u'_k u'_k}$ [m^2/s^2] on plane $y = 2$ m. Averaging time period 120 s.

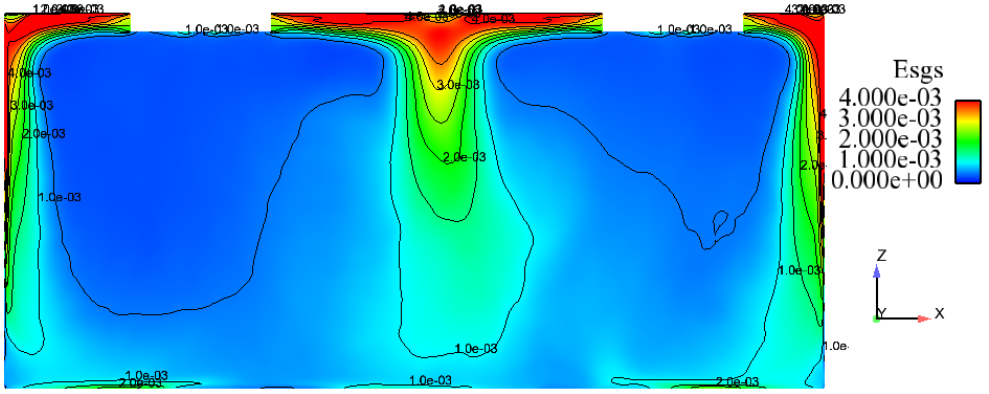

Fig. A-73: Simulation 6. Subgrid-scale turbulence kinetic energy e_{sgs} [m^2/s^2] on plane $y = 2$ m. Averaging time period 120 s.

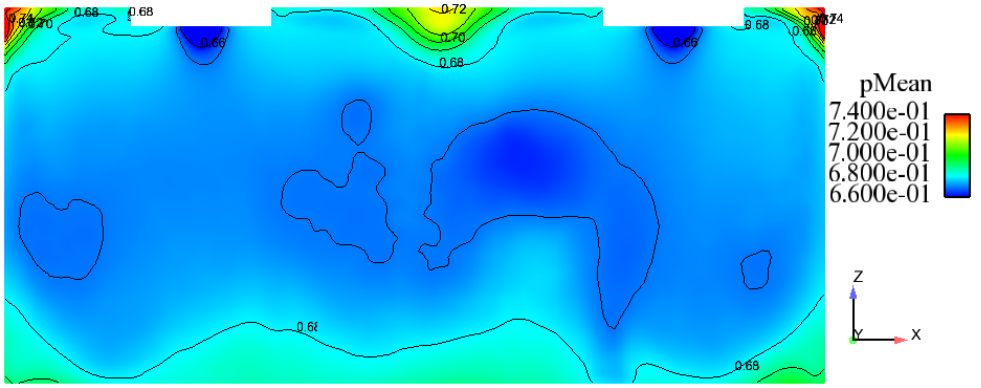

Fig. A-74: Simulation 6. Mean pressure $\overline{p}/\rho$ [m^2/s^2] on plane $y = 2$ m. Averaging time period 120 s.

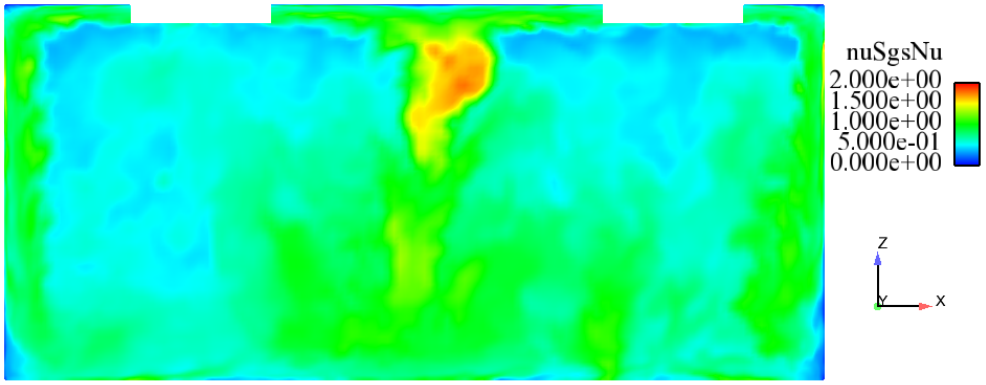

Fig. A-75: Simulation 6. Instantaneous eddy viscosity ν_{sgs}/ν on plane $y = 2$ m.

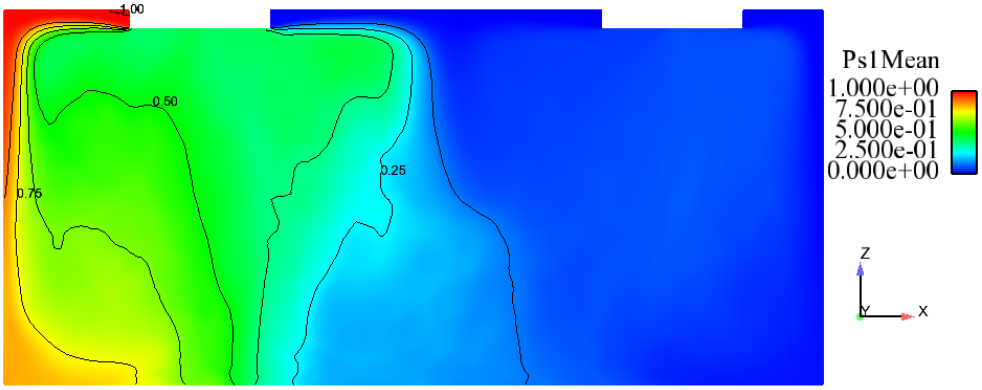

Fig. A-76: Simulation 6. Mean passive scalar $\overline{\theta}_1$ on plane $y = 2$ m. Averaging time period 120 s.

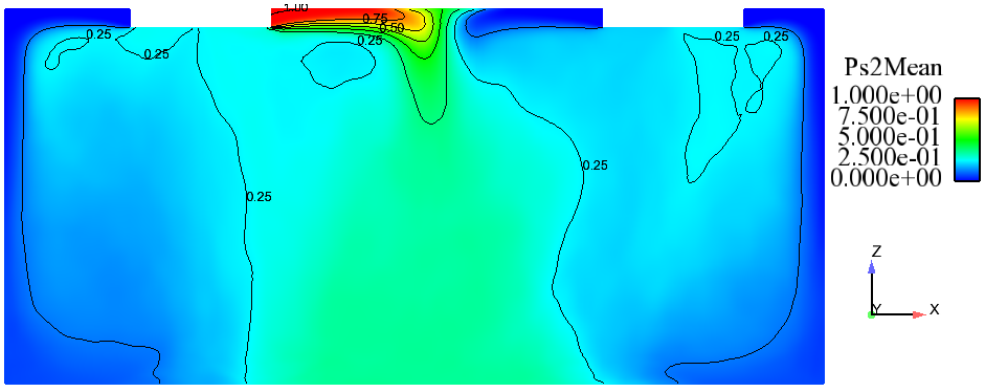

Fig. A-77: Simulation 6. Mean passive scalar $\overline{\theta}_2$ on plane $y = 2$ m. Averaging time period 120 s.

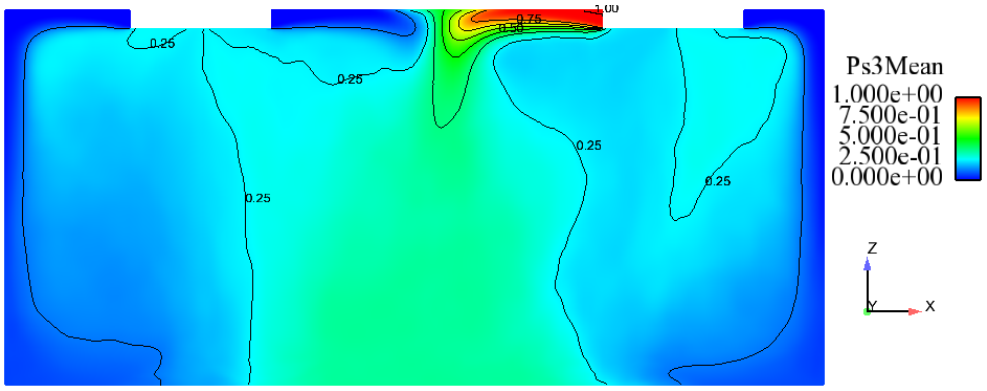

Fig. A-78: Simulation 6. Mean passive scalar $\overline{\theta}_3$ on plane $y = 2$ m. Averaging time period 120 s.

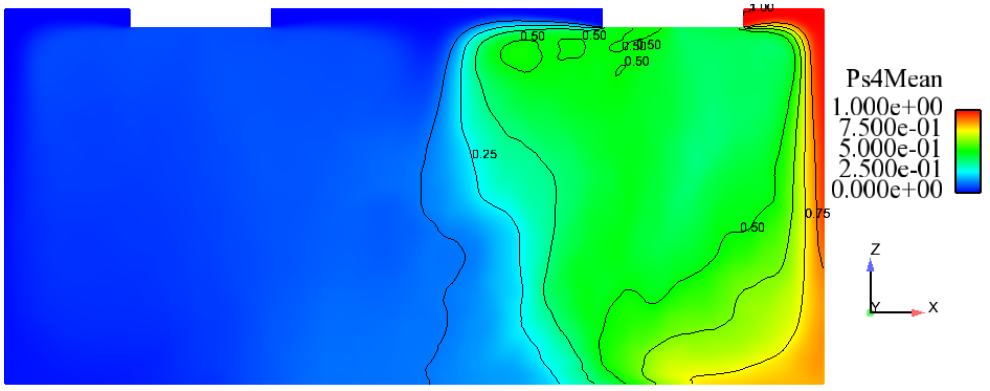

Fig. A-79: Simulation 6. Mean passive scalar $\overline{\theta}_4$ on plane $y = 2$ m. Averaging time period 120 s.

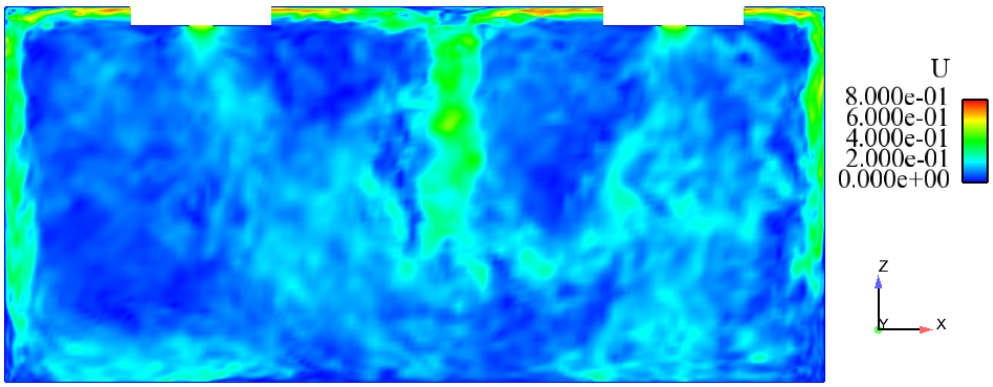

Fig. A-80: Simulation 7. Instantaneous velocity u [m/s] on plane $y = 2$ m.

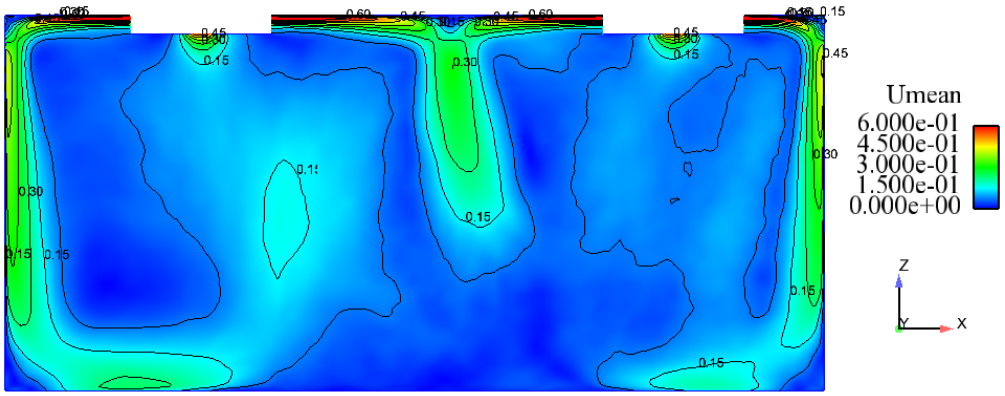

Fig. A-81: Simulation 7. Mean velocity $\overline{u}$ [m/s] on plane $y = 2$ m. Averaging time period 150 s.

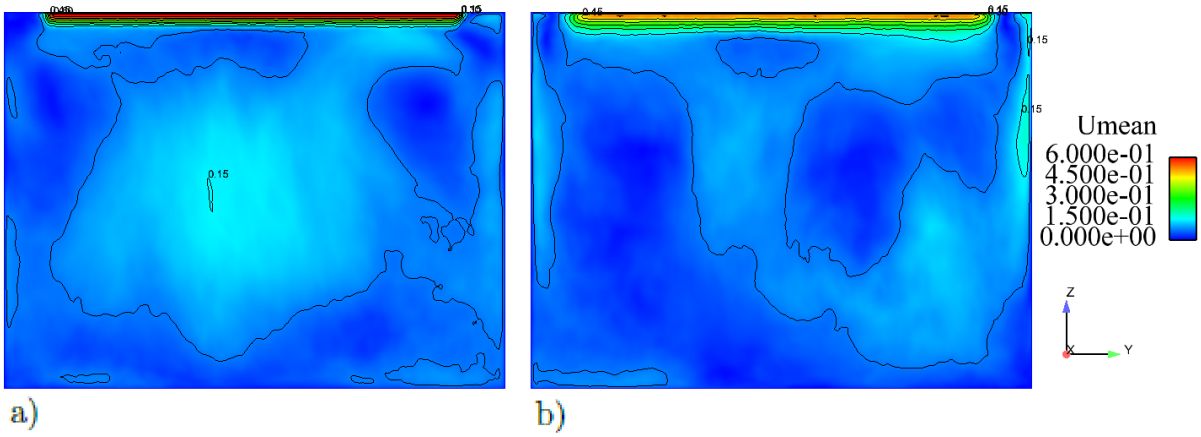

Fig. A-82: Simulation 7. Mean velocity $\overline{u}$ [m/s] on plane a) $x = 2.5$ m b) $x = 3.0$ m. Averaging time period 120 s.

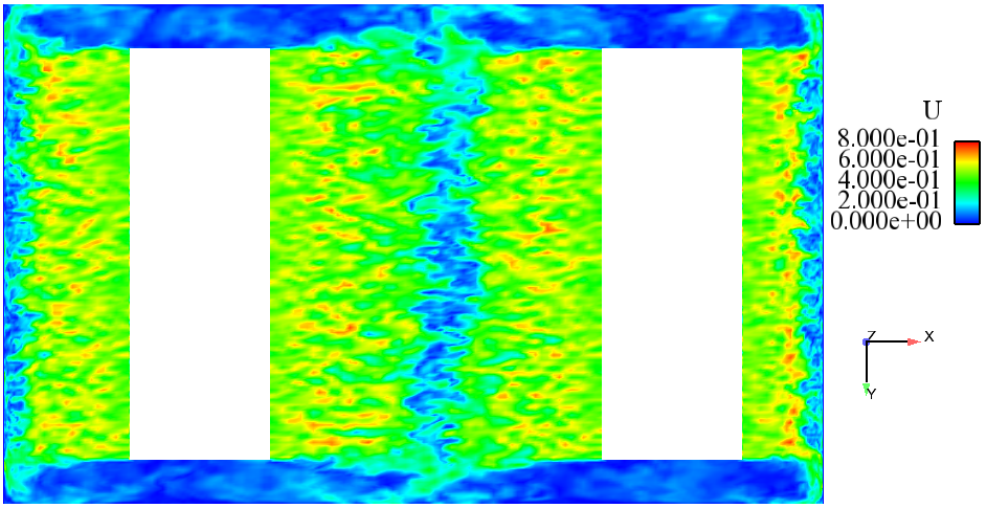

Fig. A-83: Simulation 7. Instantaneous velocity u [m/s] on plane $z = 2.95$ m.

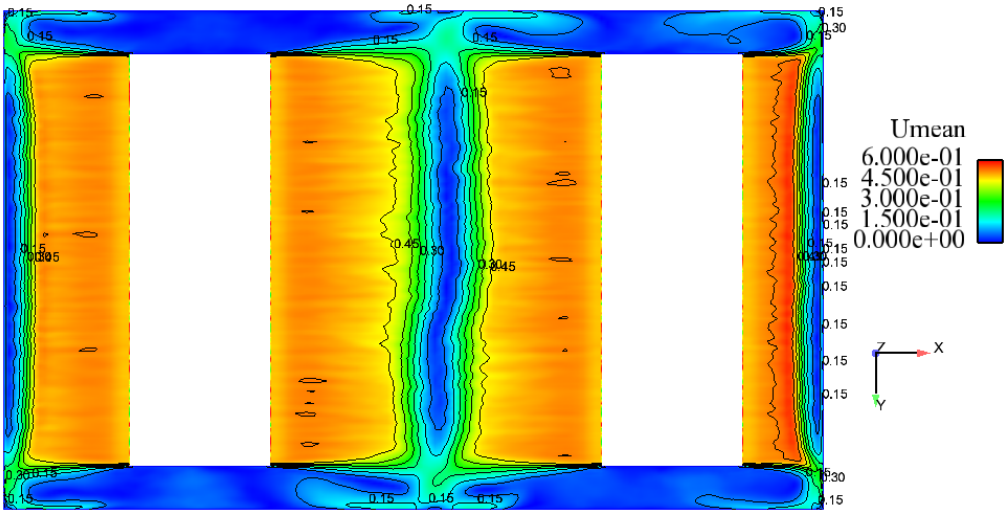

Fig. A-84: Simulation 7. Mean velocity $\overline{u}$ [m/s] on plane $z = 2.95$ m. Averaging time period 150 s.

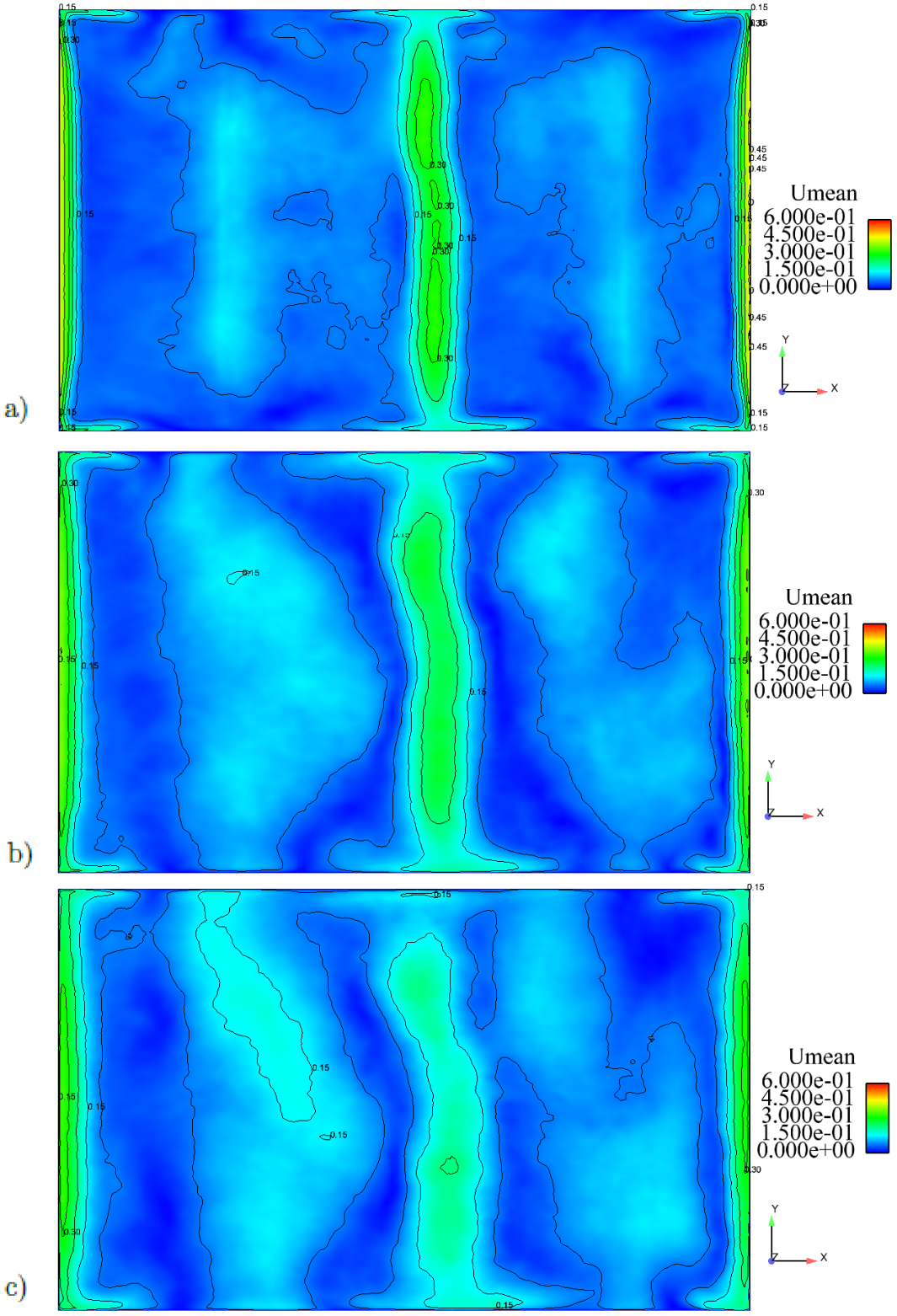

Fig. A-85: Simulation 7. Mean velocity $\overline{u}$ [m/s] on plane a) $z = 2.5$ m b) $z = 2.0$ m c) $z = 1.5$ m. Averaging time period 120 s.

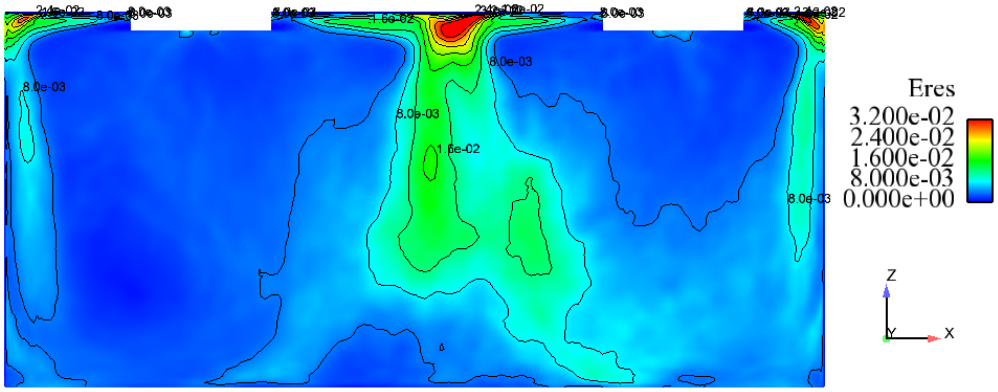

Fig. A-86: Simulation 7. Turbulence kinetic energy $\frac{1}{2}\overline{u'_k u'_k}$ [m^2/s^2] on plane $y = 2$ m. Averaging time period 150 s.

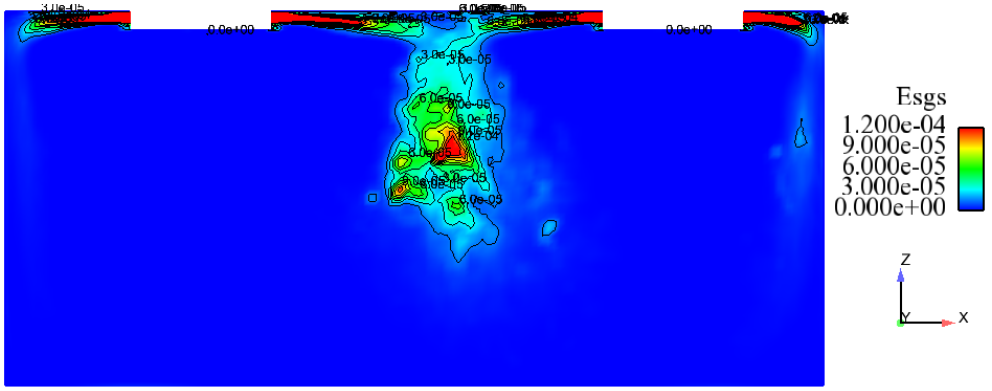

Fig. A-87: Simulation 7. Subgrid-scale turbulence kinetic energy e_{sgs} [m^2/s^2] on plane $y = 2$ m. Averaging time period 150 s.

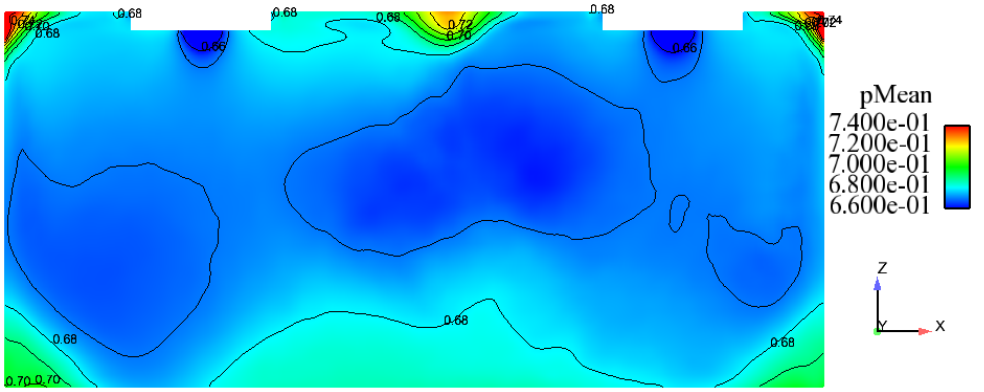

Fig. A-88: Simulation 7. Mean pressure $\overline{p}/\rho$ [m^2/s^2] on plane $y = 2$ m. Averaging time period 150 s.

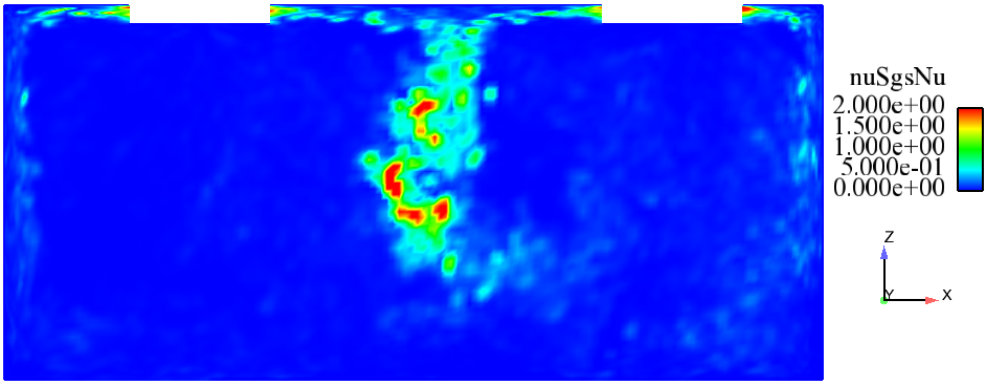

Fig. A-89: Simulation 7. Instantaneous eddy viscosity ν_{sgs}/ν on plane $y = 2$ m.

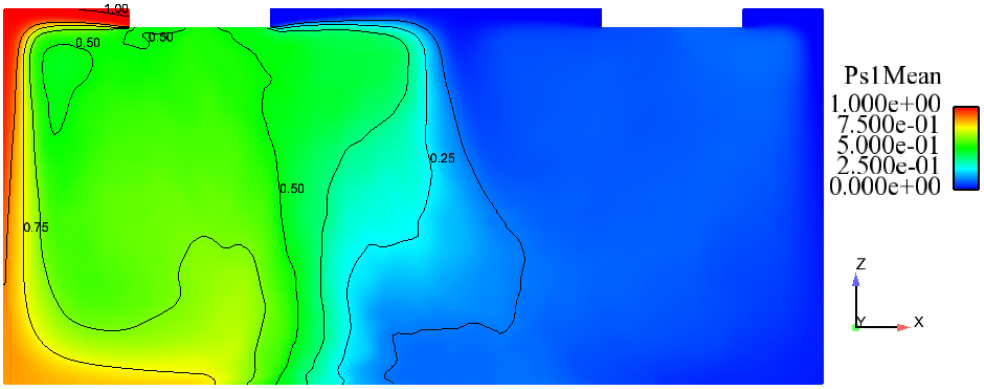

Fig. A-90: Simulation 7. Mean passive scalar $\overline{\theta}_1$ on plane $y = 2$ m. Averaging time period 150 s

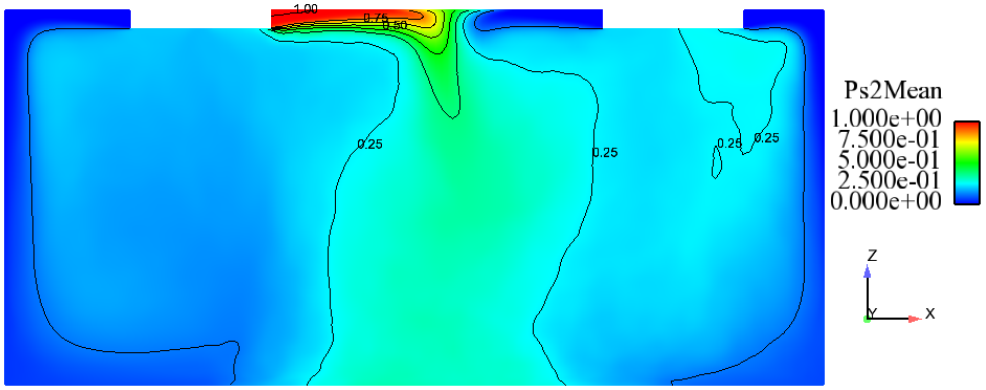

Fig. A-91: Simulation 7. Mean passive scalar $\overline{\theta}_2$ on plane $y = 2$ m. Averaging time period 150 s.

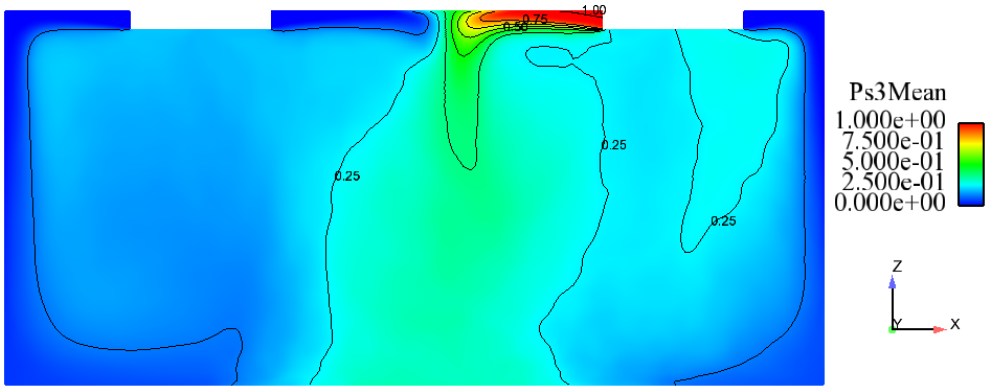

Fig. A-92: Simulation 7. Mean passive scalar $\overline{\theta}_3$ on plane $y = 2$ m. Averaging time period 150 s.

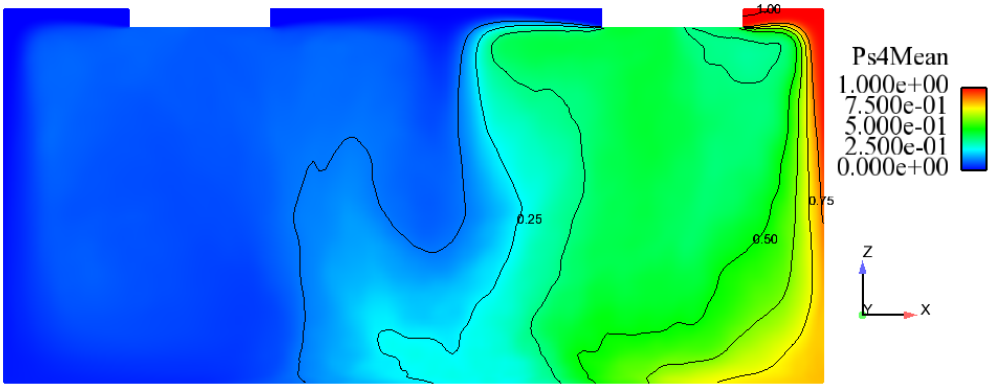

Fig. A-93: Simulation 7. Mean passive scalar $\overline{\theta}_4$ on plane $y = 2$ m. Averaging time period 150 s.